

Identifying the variety of jovian X-ray auroral
structures: tying the morphology of X-ray emissions to
associated magnetospheric dynamics

D. M. Weigt^{1,2,3}, C. M. Jackman², D. Moral-Pombo⁴, S. V. Badman⁴, C. K.
Louis², W. R. Dunn⁵, S. C. McEntee^{2,3}, G. Branduardi-Raymont⁶, D.
Grodent⁷, M. F. Vogt⁸, C. Tao⁹, G. R. Gladstone¹⁰, R. P. Kraft¹¹, W. S.
Kurth¹², J. E. P. Connerney^{13,14}

¹School of Physics and Astronomy, University of Southampton, Southampton, UK

²School of Cosmic Physics, DIAS Dunsink Observatory, Dublin Institute for Advanced Studies, Dublin,

Ireland

³School of Physics, Trinity College Dublin, Dublin, Ireland

⁴Department of Physics, Lancaster University, Bailrigg, Lancaster, UK

⁵Department of Physics and Astronomy, University College London, London, UK

⁶Mullard Space Science Laboratory, University College London, Dorking, UK

⁷Laboratory for Planetary and Atmospheric Physics, Space Science, Technologies and Astrophysical

Research Institute, University of Liège, Liège, Belgium

⁸Center for Space Physics, Boston University, Boston, MA, USA

⁹National Institute of Information and Communications Technology, Tokyo, Japan

¹⁰Southwest Research Institute, San Antonio, TX, USA

¹¹Harvard-Smithsonian Center for Astrophysics, Smithsonian Astrophysical Observatory, Cambridge, MA,

USA

¹²Department of Physics and Astronomy, University of Iowa, Iowa City, IA, USA

¹³Space Research Corporation, Annapolis, MD, 21403, USA

¹⁴NASA Goddard Space Flight Center, Greenbelt, MD, 20771, USA

Key Points:

- We present the morphology of new ‘X-ray auroral structures’, observed on Jupiter via Chandra’s high spatial resolution camera.
- Our visibility modelling of these regions show that planetary tilt has very little effect on non-uniform auroral photon distributions.
- We show that combination of X-ray and UV ‘auroral families’ may be a useful proxy to determine the magnetospheric conditions at Jupiter.

32 **Abstract**

33 We define the spatial clustering of X-rays within Jupiter's northern auroral regions by
 34 classifying their distributions into 'X-ray auroral structures'. Using data from Chandra
 35 during Juno's main mission observations (24 May 2016 – 8 September 2019), we define
 36 five X-ray structures based on their ionospheric location and calculate the distribution
 37 of auroral photons. The morphology and ionospheric location of these structures allow
 38 us to explore the possibility of numerous X-ray auroral magnetospheric drivers. We com-
 39 pare these distributions to Hubble Space Telescope (HST) and Juno (Waves and MAG)
 40 data, and a 1D solar wind propagation model to infer the state of Jupiter's magnetosphere.
 41 Our results suggest that the five sub-classes of 'X-ray structures' fall under two broad
 42 morphologies: fully polar and low latitude emissions. Visibility modelling of each struc-
 43 ture suggests the non-uniformity of the photon distributions across the Chandra inter-
 44 vals are likely associated with the switching on/off of magnetospheric drivers as opposed
 45 to geometrical effects. The combination of ultraviolet (UV) and X-ray morphological struc-
 46 tures is a powerful tool to elucidate the behaviour of both electrons and ions and their
 47 link to solar wind/magnetospheric conditions in the absence of an upstream solar mon-
 48 itor.

49 **Plain Language Summary**

50 The mechanism that allows precipitation of ions into Jupiter's atmosphere and gen-
 51 erate pulsed X-ray auroral emissions is still under debate today. Previous studies have
 52 linked this driver to possible activity in Jupiter's outer magnetosphere (the interface be-
 53 tween the solar wind and Jupiter) and have observed the emissions to exhibit variable
 54 behaviour. More recent studies have suggested a wide range of physical phenomena caus-
 55 ing these emissions. Here we explore this idea in more detail by introducing five 'X-ray
 56 auroral structures' that map to different regions in the jovian system. Using data from
 57 the Chandra X-ray Observatory during Juno's main mission allows us to calculate the
 58 distribution of X-rays from Jupiter's northern auroral region. We compare our X-ray re-
 59 sults with the ultraviolet emissions ('UV auroral families') observed from simultaneous
 60 Hubble Space Telescope (HST) data and infer the conditions at Jupiter using models and
 61 Juno observations. These 'X-ray structures' provide us with many ways to observe vari-
 62 able behaviour and provide a possible tool to monitor the solar wind conditions, when
 63 used in tandem with the HST 'UV auroral families'.

64 **1 Introduction**

65 The jovian auroral emissions are very complex and are highly variable in their mor-
 66 phological and temporal behaviour across multiple wavelengths [see full review by Badman
 67 et al. (2015) and references therein for more details]. The X-ray emissions remain the
 68 most elusive of the observable aurora with many recent studies trying to understand the
 69 highly sophisticated magnetospheric driver(s) capable of energising the ions to MeV en-
 70 ergies that allow charge stripping and charge exchange to take place in the jovian iono-
 71 sphere for soft X-ray (SXR: < 1 keV) production (e.g., Dunn, Branduardi-Raymont, et
 72 al. (2020); Dunn, Gray, et al. (2020); Houston et al. (2020)). The SXRs are produced
 73 from precipitating MeV ions originating in the outer magnetosphere and are sometimes
 74 observed to be coincident with flaring ultraviolet (UV) emissions within the UV active
 75 polar region as observed by Dunn et al. (2022) [herein refereed to as D22]. The auroral
 76 hard X-rays (HXR: > 2 keV) result from bremsstrahlung emissions from precipitating
 77 electrons, with the auroral emissions observed to sometimes coincide with the UV main
 78 emission (e.g., Branduardi-Raymont et al. (2008); Dunn et al. (2016)). This suggests that
 79 the precipitating electrons responsible for the HXR and UV main emission auroral emis-
 80 sions are likely to originate in the same region of the middle magnetosphere. Recent and
 81 ongoing studies are investigating how the X-rays are connected to other auroral emis-

sions in the EM spectrum via plasma waves such as electromagnetic ion cyclotron (EMIC) waves associated with precipitating ions, which are shown to be strongly correlated with X-ray pulsations (e.g., Yao et al. (2021)). Other studies have looked at how the HXR are correlated with the more intense UV auroral emissions (Wibisono et al., 2021), such as dawn storms - major enhancements of the UV main emission along the dawn arc with a broadening in latitude (Bonfond et al., 2021; Yao et al., 2020).

Previous studies analysing the jovian UV aurorae from the Hubble Space Telescope (HST) have isolated various regions within the auroral emissions to explore the temporal and morphological variation across them. Nichols et al. (2009) used data from two 2007 Hubble Space Telescope (HST) campaigns to identify three northern UV auroral components: (1) the main oval (main emission), (2) low-latitude and (3) high-latitude auroral emissions. They calculated the auroral power, via analysis of the observations and visibility modelling of each region, and predicted solar wind conditions propagated from Earth to investigate the most likely cause of variation. Their results showed that generally the auroral power from the polar regions (low- and high- latitude auroral emissions) were uncorrelated with that of the main emission unless a dawn storm or enhancements due to a magnetospheric compression occurred. This may be a result of the polar emissions, in particular the swirl region observed to contain patchy and turbulent auroral emissions at the centre of the UV polar auroral emissions, having a strong local time dependence (Greathouse et al., 2021).

Nichols et al. (2017) followed up their previous study by segmenting the northern auroral region further, focusing on four regions of interest. These regions were applied to a larger HST dataset (around 47 orbits in total), covering May to July 2016 during Juno's (Bolton et al., 2017) final approach to Jupiter and its orbit insertion in the dawn flank of Jupiter's magnetosphere. By comparing the Juno *in situ* interplanetary data (McComas et al., 2017) and the HST UV auroral images they observed the intensity of the the main emission (at System III (SIII) longitudes $> 170^\circ$) to increase for 1 - 3 days following compression events identified by Juno, with emissions on the polar dusk side to also brighten during these times and during shallow rarefactions of the solar wind. Auroral emissions equatorward of the main emission (at SIII longitudes $< 190^\circ$) brightened ~ 10 days following enhanced Io plasma torus emissions observed from the EXtreme ultraviolet spectrosCope for ExosphEric Dynamics (EXCEED) on board Hisaki (Yoshioka et al., 2013). The noon active region did not show any clear correlation between intensity and interplanetary conditions, although the morphology was observed to change between periods of rarefactions and compressions. The variability of these emissions across the specific regions highlights how the auroral and magnetospheric dynamics change across different local times.

More recently, Grodent et al. (2018) [herein referred to as G18] characterised HST images during Juno orbits 3 to 7 (from 30 November 2016 up to and including 18 July 2017), using six new definitions of "UV auroral families" to help provide a simplified description of the complex dynamics observed in the UV auroral emissions: (1) Q (or 'quiet') has a very low auroral power (< 1 TW) with a lower latitude main emission (ME); (2) N has a 'narrow' and expanded ME, exhibiting average power; (3) U describes more 'unsettled' conditions and is the intermediate behaviour between Q and N ; (4) I is associated with strong injections with a 'corner-like' morphology, located at ionospheric dusk with (5) more moderate injections being represented by the i family. (6) The final family, X , is linked to 'eXternal' perturbations generating very strong and contracted ME with large enhancements at dawn and strong, narrow auroral arcs in the afternoon-dusk sector. Such behaviour is usually observed during solar wind compressions. These new definitions allowed different morphologies to be compared to establish logical, plausible connections to identify the responsible auroral driver and allowed a more detailed quantitative way to analyse variations of spatial behaviour. G18 observed that auroral emissions corresponding to the U family occurred most often (29.5% of 118 HST images)

and were identified to be connected to the Q family due to slight changes in brightness of the ME. The connection was only interrupted by episodes of injection events (I, i) which were observed to precede or follow the N family. The moderate injections, i , were identified after auroral structures associated with compressions of the interplanetary medium (X). The disturbances from compressions can trigger episodic injections of trapped particles in the middle magnetosphere, as observed by Louarn et al. (2014) from Galileo particle and radio measurements. More details of the UV auroral families described here can be found in G18. Yao et al. (2020) found that dawn storms and injection events were correlated with intervals of tail reconnection and dipolarization.

In this study, we utilise the techniques used for the UV auroral emissions to isolate and define specific auroral structures and apply them to the concentrated northern X-ray emissions in an attempt to find a link between X-ray morphology and magnetospheric dynamics. We use concurrent HST data to help provide vital magnetospheric context to the Chandra (Weisskopf et al., 2000) observations, using the G18 auroral definitions, and model the visibility of the X-ray auroral structures we define here, similar to Nichols et al. (2009). We then compare the magnetospheric dynamics found from the X-ray-UV data and compare with the magnetospheric conditions identified from the Juno spacecraft, using radio (Kurth et al., 2017) and magnetometer (Connerney et al., 2017) data. This allows us to determine the state of the jovian magnetosphere and to compare against the solar wind predictions of the Tao et al. (2005) 1D magnetohydrodynamic (MHD) solar wind propagation model. Similar to the logic applied by G18, the goal of this study is to simplify the complex morphological variations of the X-ray aurora, allowing plausible connections to be made between the auroral emissions and magnetospheric dynamics. Linking our X-ray structures with the UV equivalent may provide additional context from which to infer the state of the jovian magnetosphere in the absence of upstream solar wind data.

Previous observations noted morphological variations in the X-ray aurora and attempted to connect this with solar wind conditions for a limited sample of observations taken in 2007 and 2011, for which interpretation was further challenged by limitations on viewing geometry (Dunn et al., 2016; Dunn, Branduardi-Raymont, et al., 2020; Dunn, Gray, et al., 2020). The work here, with a more comprehensive observation dataset supported by *in situ* insights from the Juno spacecraft, may also help to put these historic X-ray observations into context.

2 Contemporaneous remote sensing UV and X-ray observations with Juno Waves and MAG data

We use the catalogue of Chandra HRC-I (High Resolution Camera - Imaging: 30 arcmin \times 30 arcmin field of view, with pixel size 0.13 arcsec and spatial resolution of 0.4 arcsec) observations defined and tabulated in Weigt, Jackman, et al. (2021), focusing on those taken during the Juno main mission (24 May 2016 up to and including 8 September 2019). The Chandra observations used here are a combination of HXRs and SXRs due to the very limited spectral resolution of HRC-I, meaning that we cannot segregate photons of these two energy regimes. However, previous work suggested that greater than 90% of the observed X-ray photons detected by Chandra ACIS (Advanced CCD Imaging Spectrometer) were soft X-ray photons Dunn, Branduardi-Raymont, et al. (2020) and the energy response of HRC is softer than ACIS, so that we expect the majority of detected X-ray photons to be produced by precipitating ions. These observations include those taken during Juno's approach to Jupiter (in the solar wind), while Juno was at apojove (near the dawn magnetopause), during several perijoves and intervals when Juno was inside and crossed the jovian plasmashell. We then correct the Chandra observations using the updated mapping algorithm described in McEntee et al. (2022), assuming the altitude of X-ray emissions is 400 km above the 1-bar atmosphere, to ensure that we have accounted for the time-dependent degradation of the Chandra HRC-I instru-

Table 1. Table of concurrent Chandra and HST observations throughout the Juno era. Date and time of each observation, identified UV auroral families from current literature using the G18 definition and predicted solar wind dynamic pressure from the Tao et al. (2005) model with average Jupiter-Sun-Earth angle are shown. Bold entries highlight observations associated with possible eXternal perturbation (X) structures. Solar wind parameters determined over a 2 day window centered on the Chandra observation to account for propagation errors within Tao et al. (2005) model. Each Chandra observation is labelled with a unique Observation ID (ObsID).

Observation start date (dd/mm/yyyy)	Chandra ObsID	Observation interval (Juno time; light corrected)		HST UV northern auroral family*		Mean solar wind† P_{dyn} (nPa)	Max solar wind† P_{dyn} (nPa)	Mean Jupiter-Sun- Earth angle† (°)
		Chandra	HST	G18 ^a	This study			
24/05/2016	18608	09:39 - 20:41	17:03 - 17:47 20:14 - 20:58	-	U	Q/N U	0.006	0.007 ~ 57.7
01/06/2016	18609	10:47 - 21:49	14:13 - 14:57 17:24 - 18:08	-	U	Q/N Q/N	0.138	0.309 ~ 64.6
02/02/2017	18301	09:14 - 18:19	16:17 - 16:57	-	i	i	0.009	0.015 ~ -79.9
28/02 (Chandra); 01/03/2017 (HST) ^c	20000 ^c	11:58 - 07:34	14:37 - 15:16	i	i	-	0.019	0.024 ~ -53.3
18/05 - 19/05/2017	18302	23:48 - 10:10	04:27 - 05:07 06:03 - 06:43	N	N	N N	0.052	0.148 ~ 19.2
18/06/2017^c	20001^c	17:55 - 04:06	08:31 - 09:13	X	i	-	0.090	0.230 ~ 47.9
06/08/2017 ^d	20002 ^d	01:07 - 10:50	-	-	-	-	0.015	0.024 ~ 99.0
01/04/2018	18678	09:59 - 21:06	09:59 - 10:17	-	X	-	0.116	0.275 ~ - 58.4
23/05 - 24/05/2018	18679	23:22 - 10:21	09:02 - 09:32	-	U	Q	0.049	0.115 ~ -3.6
06/09/2018	18680	19:50 - 06:56	04:22 - 05:02	-	i	X	0.056	0.086 ~ 97.0
29/05/2019	22159	02:50 - 12:34	12:18 - 12:56	-	i	-	0.014	0.019 ~ -32.5
15/07/2019	22148	12:21 - 19:13	14:06 - 14:44	-	U	N	0.068	0.115 ~ 10.5
16/07/2019	22149	08:07 - 15:00	10:43 - 11:21	-	U	Q	-	~ 11.3
18/07/2019 ^c	22150 ^c	19:40 - 01:32	14:10 - 14:49	-	i	N	0.057	0.096 ~ 13.9
08/09/2019	22151	08:01 - 14:46	14:24 - 15:02	-	X/i	-	0.262	0.879 ~ 64.0

* UV families as described in Grodent et al. (2018)

† Predicted values from Tao et al. (2005) model over 2 day window centered on Chandra observation

^a UV families identified from Grodent et al. (2018) (G18)

^b UV families identified from Dunn et al. (2022) (D22).

^c observations not concurrent but occurred ± 1 day from Chandra interval.
^d inferred compression from Juno data, no HST data.

187 ment while removing any contaminant background (Weigt et al., 2022). Here our focus
 188 is on the brightest and most concentrated X-ray northern auroral emissions, located us-
 189 ing the Weigt et al. (2020) numerical criterion of >7 photons per $5^\circ \text{ SIII longitude} \times 5^\circ$
 190 latitude over ~ 10 hours (the average duration of the observations of the catalogue, around
 191 a jovian rotation). We note using this more updated mapping method provides minimal
 192 change in X-ray count rates from the Weigt, Jackman, et al. (2021) study and therefore
 193 does not change the interpretation of these results. We highlight here that accounting
 194 for the instrument's increasing degradation (and particle background) is crucial for fu-
 195 ture studies during the Juno extended mission (especially when mapping X-ray emissions
 196 to the jovian disk). The degradation of HRC-I has also been observed when analysing
 197 time-tagged photon data in a low-count regime from Saturn (Weigt, Dunn, et al., 2021).

198 To help provide essential magnetospheric context to the X-ray auroral emissions,
 199 we use HST observations concurrent with Chandra data. We analyse 17 Chandra ob-
 200 servations during the Juno-era, 14 of which have HST Space Telescope Imaging Spec-
 201 trograph (STIS: $24.7 \text{ arcsec} \times 24.7 \text{ arcsec}$ field of view, spatial resolution of 0.0025 arc-
 202 sec) data ± 1 day from the Chandra window, to allow the magnetospheric conditions to
 203 be analysed in detail. STIS detects far ultraviolet (FUV) auroral emissions of wavelengths
 204 $\sim 130 - 180 \text{ nm}$ (photon energies $\sim 7 - 10 \text{ eV}$) using the F25SRF2 filter to eliminate geo-
 205 coronal Ly- α contamination and to reduce the reflected sunlight from the jovian disk (e.g.,
 206 Grodent (2015)). These 14 HST observations focus on the northern auroral emissions
 207 of which components within the UV aurora have been identified using the G18 defini-
 208 tions. We note that we add to this catalogue with three newly identified HST observa-
 209 tions coinciding with Observation ID (ObsID) 22159 (29 May 2019), 22150 (18 June 2019)
 210 and 22151 (8 September 2019). All observations used in this research are shown in Ta-
 211 ble 1. To compare with contemporaneous Juno data, both the Chandra and HST inter-
 212 vals have been corrected for the Juno-Earth light-travel time, taken from ephemeris data
 213 obtained via the JPL Horizons database (data available at <https://ssd.jpl.nasa.gov/horizons/app.html#>). The mean and max dynamic pressure (P_{dyn}) estimated from the
 214 Tao et al. (2005) 1D MHD model over a 2 day window centered on the Chandra inter-
 215 val with the corresponding average Jupiter-Sun-Earth (JSE) angle are also given in Ta-
 216 ble 1. This 2-day window is used for all observations irrespective of JSE angle to account
 217 for propagation and interpolation errors. We note that Chandra observations taken be-
 218 yond 8 September 2019 (and after the creation of the Weigt, Jackman, et al. (2021) cat-
 219 alogue) have no direct overlap with any HST campaigns and are therefore not included
 220 in this study.

222 We then compare these observations to remote sensing radio data (spectrograms)
 223 from Juno Waves and *in situ* data (time series) from the magnetometer, Juno MAG to
 224 confirm the magnetospheric state during these intervals and potentially identify any
 225 internal magnetospheric drivers (e.g. such as particle injection signatures). Juno's eccen-
 226 tric polar orbit allows it to sample the inner, middle and outer magnetosphere during
 227 its 53-day orbit, providing us the opportunity to analyse the different internal auroral
 228 drivers, hence the auroral emissions, located throughout the jovian magnetosphere. We
 229 take this into account when interpreting these data.

230 3 Results

231 Following studies that have identified different regions within the UV emissions as-
 232 sociated with different potential drivers (e.g., Grodent et al. (2018)), we apply similar
 233 logic to the X-ray northern auroral emissions from the Weigt, Jackman, et al. (2021) Chan-
 234 dra catalogue during the Juno-era. Here we use the families defined from UV emissions
 235 from concurrent HST observations to provide vital context to the concentrated north-
 236 ern X-ray emissions and use the superior spatial resolution of HST-STIS to model the
 237 visibility of each X-ray auroral region.

238 **3.1 Identifying X-ray auroral structures**

239 As analyzed in the statistical study by Weigt, Jackman, et al. (2021), it is clear that
 240 the northern X-ray emissions exhibit large variations in morphological and temporal be-
 241 haviours with only a very small region of X-rays appearing across the entire ~ 20 year
 242 Chandra HRC-I dataset: the averaged hot spot nucleus (AHSNuc), mapping to the noon
 243 magnetopause boundary. We show examples of 2D histograms of mapped concentrated
 244 X-rays, using the Weigt et al. (2020) numerical criterion, in Figure 1 within the *X-ray*
 245 *noon* region (red), where the colour bar shows the photon flux of the X-rays (counts s $^{-1}$)
 246 and the 1D histograms show the latitude (lat) and System III longitude (SIII lon) dis-
 247 tribution of the X-ray emissions. Similar to the ‘Region X’ defined in D22, the X-ray noon
 248 region contains both the UV swirl and active regions (Grodent et al., 2003) and there-
 249 fore the X-ray emissions they may generate. The remaining X-ray auroral structures we
 250 define here are *X-ray dusk* (purple), *X-ray dawn* (gray), the *Low Latitude Extension re-
 251 gion* (LLE; gold), equatorward of X-ray noon and the *X-ray polar region* (striped region)
 252 which envelopes both the noon and dusk structures. The statistical UV main emission
 253 (accounting for a compressed and expanded magnetosphere) and Io and Ganymede mag-
 254 netic footprints taken from Bonfond et al. (2017) are also plotted to provide context of
 255 the location of these regions within the magnetosphere. The coordinates of each region
 256 (in SIII lon, lat) are given in the Supplementary Information (SI: see Data Set S1).

257 In Figure 1 (covering a central meridian longitude (CML) of 110° - 220°), we show
 258 four examples of different auroral morphologies each under different conditions: (a) where
 259 all auroral emissions are within the polar region (ObsID 18301: 2 February 2017); (b)
 260 where the most intense auroral emissions are observed to be shifted equatorward (Ob-
 261 sID 22151: 8 September 2019); (c) auroral morphology during a compressed magneto-
 262 sphere (ObsID 20001: 18 June 2017) and (d) an observation during Juno a apojove (Ob-
 263 sID 18678: 1 April 2018). Three out of the four cases show the majority of the concen-
 264 trated, and most intense, X-ray emissions are located in the X-ray polar region, dom-
 265 inated by X-ray noon. These emissions are therefore likely to be co-located (and pos-
 266 sibly linked) with the UV activity in the polar and swirl regions and possibly coincide
 267 with flaring UV emissions (e.g., Elsner et al. (2005); Dunn (2022)). Previous studies (e.g.,
 268 Grodent et al. (2003); Grodent (2015); Greathouse et al. (2021) and references therein)
 269 have also identified the polar active region as the most dynamic of the UV polar emis-
 270 sions, producing flares and bright arc sub-structures of a few hundred kilo-Rayleigh (kR)
 271 lasting in the order of a few minutes. The examples shown in Figure 1 are discussed fur-
 272 ther in the remainder of Section 3.

273 The X-ray dawn region is found to coincide with a portion of the main emission
 274 and the Io footprint suggesting an association between dawn storms, injections of hot
 275 plasma from the middle magnetosphere (e.g., Gerard et al. (1994); Kimura et al. (2017))
 276 and bright X-ray populations. Recent work by Wibisono et al. (2021) found the inten-
 277 sity of the HXRs to increase during the presence of a dawn storm with reduced activ-
 278 ity from the more poleward SXRs, utilising the energy resolution of XMM-Newton. Re-
 279 gions of X-ray dawn at higher latitudes are likely to overlap with the UV dark polar re-
 280 gion (DPR) which contains very little UV emissions and is observed to contract and ex-
 281 pand as Jupiter rotates, mapping to the outer magnetosphere (e.g., Pallier and Prangé
 282 (2001); Grodent et al. (2003); Swiethenbank-Harris et al. (2019)). The DPR has been found
 283 to be the likely location of empty flux tubes, emptied via Vasyliūnas-like reconnection
 284 in the tail which then rotate to the dayside magnetosphere (Vasyliūnas, 1983), result-
 285 ing in very little UV emissions here. Recent work by D22 found that the DPR is also
 286 present within the X-ray northern auroral emissions. D22 deduced from Chandra and
 287 HST observations (and simulated data) that very few or no X-ray photons are to be lo-
 288 cated in the DPR. They confirm this conclusion from their Monte Carlo simulations which
 289 state that the likelihood of X-rays being emitted from the DPR is very small, including

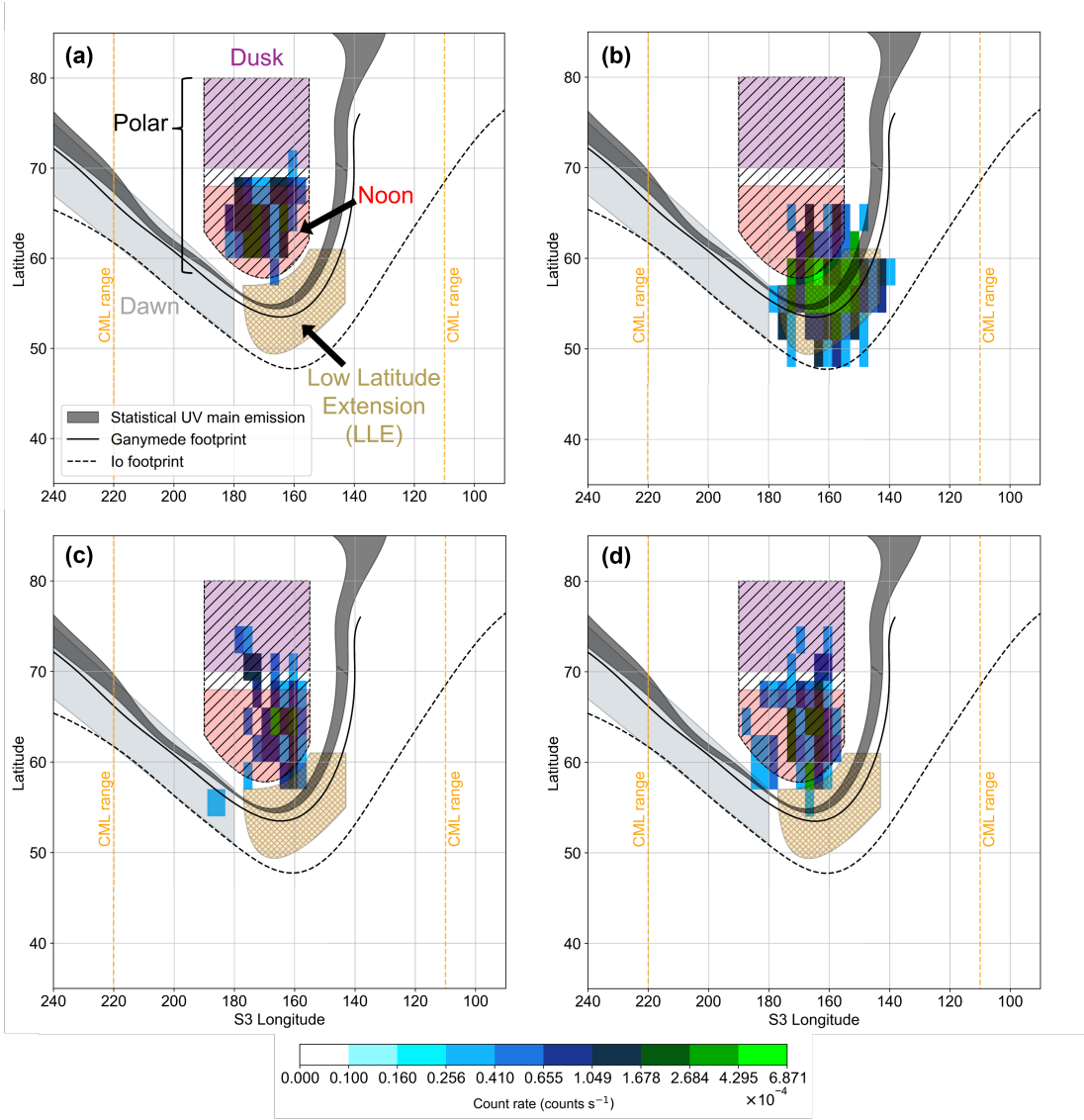


Figure 1. A Cartesian plot of the X-ray mapping for four example Chandra observations analysed in this research, each under different conditions: (a) ObsID 18301 (2 February 2017), where all auroral emissions are within the polar region; (b) ObsID 22151 (8 September 2019), where the auroral emissions are shifted equatorward; (c) ObsID 20001 (18 June 2017), auroral morphology during a compressed magnetosphere and (d) ObsID 18678 (1 April 2018), CXO observation during Juno apojove. Each case is expanded upon in the remainder of Section 3. The location of the X-ray auroral structures as described in the text (red: noon; purple: dusk; gray: dawn; gold: LLE; striped: polar) are shown in each panel and are labelled in (a). The count rates (counts s^{-1}) of the concentrated X-ray auroral emissions (2D histogram: binned by 3° SIII lon \times 3° lat) are given by the colour bar. The statistical UV main emission accounting for compressed and expanded states (dark gray shading), and the footprints of Io (black-dashed line) and Ganymede (solid black line) are overplotted (Bonfond et al., 2017). The X-ray emissions mapped and analysed for this research are selected from a 9000 ± 1080 s interval, covering a central meridian longitude (CML) range of $110^\circ - 220^\circ$ (i.e. optimum visibility for each region as shown in Figure 2). This CML range is overplotted with orange dashed lines.

290 possible scattering of solar X-ray photons in the jovian upper atmosphere as an explanation
291 for the sporadic and very dim X-ray emissions in the Dark region.

292 The regions likely to contain more extreme cases of auroral activity are the X-ray
293 dusk (see Figures 1 (c) and (d)) and LLE regions (Figure 1 (b)) where the brightest emis-
294 sions may span poleward or equatorward of the nominal position as found by Weigt, Jack-
295 man, et al. (2021), where it was observed that concentrated X-ray photons are occasion-
296 ally (30 - 70% occurrence) found at latitudes between 54° and 75° . Therefore these re-
297 gions will likely contain rare auroral morphologies linked to more unusual or extreme mag-
298 netospheric dynamics. The LLE region covers an area of UV auroral emissions possibly
299 associated with active particle injections from the middle magnetosphere driven by re-
300 connection events and dipolarizations of the jovian magnetic field (e.g., Dumont et al.
301 (2014, 2018); Yao et al. (2020)). Such injection events are found to occur alongside dawn
302 storms, suggesting disturbances of the middle magnetosphere at a range of local times
303 (e.g., Gray et al. (2016)). The 2-D histograms for all observations analysed and corre-
304 sponding plots highlighting the filtering performed on the concentrated X-ray lightcurves
305 photons using our CML criterion can be found in the SI (Figures S1 and S2).

306 3.2 Visibility and distribution of auroral photons across the X-ray au- 307 roral structures

308 The tilt of Jupiter, as viewed from the observer, can lead to issues of viewing ge-
309 ometry of the planet when using remote sensing data (e.g., Dunn et al. (2017); Dunn,
310 Branduardi-Raymont, et al. (2020); Weigt, Jackman, et al. (2021)). As the magnetic field
311 at the South pole is more dipolar, this tilt of the planet affects these emissions the most
312 when viewed from Earth. However we cannot completely neglect such effects when view-
313 ing the northern emissions as the longitude of the observer (or CML) can change what
314 parts of the emissions are observed. To resolve such issues, we utilise the higher spatial
315 resolution of the HST-STIS instrument compared to Chandra to model the visibility of
316 each X-ray auroral structure, using the area of the region defined in SIII lon and lat as
317 they rotate into view of HST-STIS. We use the number of visible pixels of each X-ray
318 region as it rotates into view as a proxy to gauge the visibility of our X-ray structures
319 as viewed by an observer at Earth. In other words, we analyse how much of an effect the
320 tilt of the planet has when observing fixed regions (in SIII lon and lat) on Jupiter from
321 any Earth-based instrument. We define the visibility here as the number of visible STIS
322 pixels associated with each X-ray region during one jovian rotation. We assume that the
323 emissions across the area of the defined X-ray structures used in the model were uniform.

324 We adopt the method of Nichols et al. (2009) used to measure the visibility (as a
325 function of normalized power) of different isolated components of UV auroral emissions
326 during two HST campaigns in 2007, using the Advanced Camera for Surveys (ACS) So-
327 lar Blind Channel (SBC). Here we apply this algorithm to the X-ray structures, using
328 the ionospheric position and size of each region as viewed by HST-STIS (with greater
329 resolution than Chandra). Figure 2 shows the results of our visibility modelling over a
330 full jovian rotation (e.g. full CML coverage) for the highest (orange: -3.39°) and low-
331 est (black: $= -1.52^\circ$) sub-Earth latitude during the Juno main mission for all X-ray au-
332 roral structures. The sub-Earth latitude relates to how tilted Jupiter is away from the
333 observer, resulting in the peak for both cases being different. Here, we define the visi-
334 bility as the number of pixels visible for each of the X-ray regions normalized to the max-
335 imum for the lowest planetary tilt case. The CML range (110° to 220°) used through-
336 out this study is also overplotted in light-blue.

337 The location of peak visibility in all panels is associated with the optimum CML
338 of which the full region is in view and is therefore related to the ionospheric position of
339 the X-ray structure. The width of the peak gives an indication of the size of the region
340 of interest. As shown in Figure 2, the location and width of the modelled peak visibil-

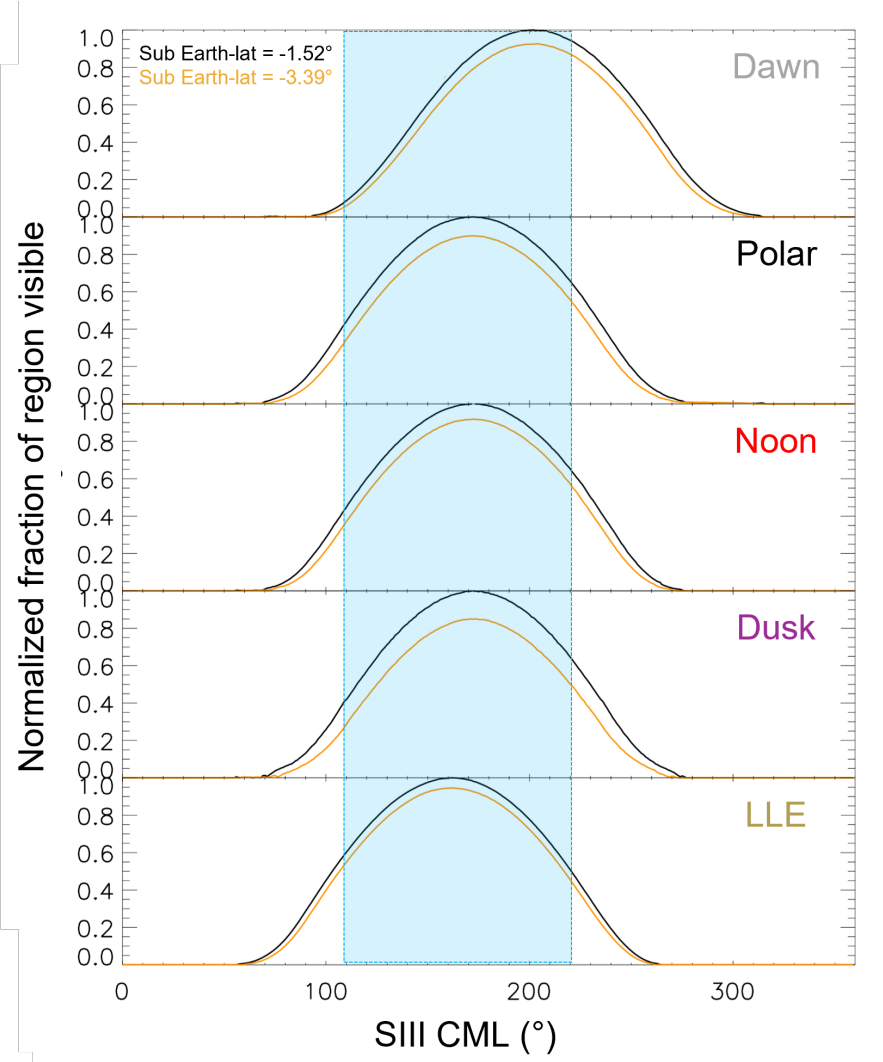


Figure 2. Plot showing the modelled normalized visibility for a full jovian rotation of each northern auroral region as observed from STIS on board HST. We model the visibility during the smallest (black: $= -1.52^\circ$) and largest (orange: -3.39°) planetary tilt as viewed from Earth (sub-Earth latitude) during the Juno main science mission. The CML range used to analyse the concentrated X-ray emissions is overplotted with the light-blue shaded area. The number of pixels visible for each region is normalised to the maximum for the sub-Earth latitude $= -1.52^\circ$ case.

ity for the polar, noon and dusk regions (labelled with the same colours corresponding to the regions in Figure 1) are very similar as expected as all regions span the same SIII ion range. The main discrepancies are associated with the amplitude of the peak with the dusk region having the fewest number of visible pixels resulting from the region being more poleward and more difficult to view with HST-STIS [see Grodent (2015) for more details] and therefore more sensitive to sub-Earth latitude. The peak visibility of all the X-ray auroral structures lie within our CML range and therefore likely associated with the peak of the X-ray light curve of the northern emissions. We note X-ray noon is also affected by sub-Earth latitude to an extent, but the normalized fractional visibility still remains above 0.8 (i.e. > 80% of all pixels visible to noon) during the more restricted viewing geometry. Since the polar region is the accumulation of visible pixels from both X-ray noon and dusk, the modelled visibility curve is, as expected, a combination of both regions. The dawn region spans greater longitudes and surrounds the polar emissions, following a portion of the dawn main emission leading to the peak visibility shifting to higher CMLs. As the shape of X-ray dawn region is longer in size (i.e. spans a greater range of longitudes) the peak of the visibility curve is broader, as it is less sensitive to the tilt of the planet. This region is more equatorward than the X-ray polar region. This is similar for the LLE region, although this auroral structure spans the smallest range of longitudes out of the X-ray structures which is reflected by the width of the visibility curve. Although none of these results are particularly surprising, this is the first time the visibility of the X-ray auroral emissions has been modelled in this way.

The distributions of auroral X-ray photons within each of the auroral structures for each Chandra observation are shown as a stacked bar chart in Figure 3, with the ObsIDs in order of observation start date (as shown in Table 1) throughout the duration of Juno's main mission. Each region is represented by the same colours and labels used in Figure 1 with all four examples indicated by a black arrow. The mean number of total auroral photons populating the X-ray structures, μ , is given by a horizontal dashed line with a value 92.92%. In other words, $\sim 93\%$ of northern X-ray auroral emissions are likely to be located within the described X-ray regions. Observations where the sum of the components are $< 100\%$, as shown in Figure 3, indicate that concentrated emissions were also mapped to regions outside the X-ray auroral structures. The X-ray emissions used in the stacked bar chart, and mapped using the 2D histogram in Figure 1, span the same CML interval ($110^\circ - 220^\circ$) including the peak visibility of all regions. As many of the X-ray observations have different exposure times, this ensures we are removing any observation bias as the same portion of all northern auroral emissions is observed in each of the Chandra campaigns.

As shown by the highlighted example [introduced in Figure 1 (a): ObsID 18301] in Figure 3 and three other observations (ObsID 20002 (no HST intervals during this time), 18679 and 18680; details of the observations in Table 1), $\geq 95\%$ of concentrated northern auroral emissions are located within the X-ray polar region, and are dominated by X-ray noon photons. During these intervals there were no dawn or LLE region photons detected despite these regions being in view of Chandra at the time. However, many other observations have auroral photons located in this range within the same viewing and timing restraints. This therefore suggests that the potential drivers that cause emissions in these regions may be "switched off". Further evidence of this is shown by the observations that had a higher population of LLE photons ($> 10\%$ of total photons) with no X-ray dusk emissions (ObsID 18608, 18677, 22148, 22150 and 22151). This suggests that during these intervals, the concentrated X-ray emissions were located equatorward of the main emission and displaying more extreme morphological behaviour when compared to the averaged map of northern auroral emissions (Weigt, Jackman, et al., 2021). This is shown by the low occurrence rate of the X-ray emissions (using the same SIII ion/lat binning). The most extreme example, ObsID 22151 (8 September 2019: Figure 1b)), is a very rare case of the majority of the auroral emissions mapping to beyond the polar region. Examples where the auroral emissions span the LLE and X-ray dusk regions (e.g.,

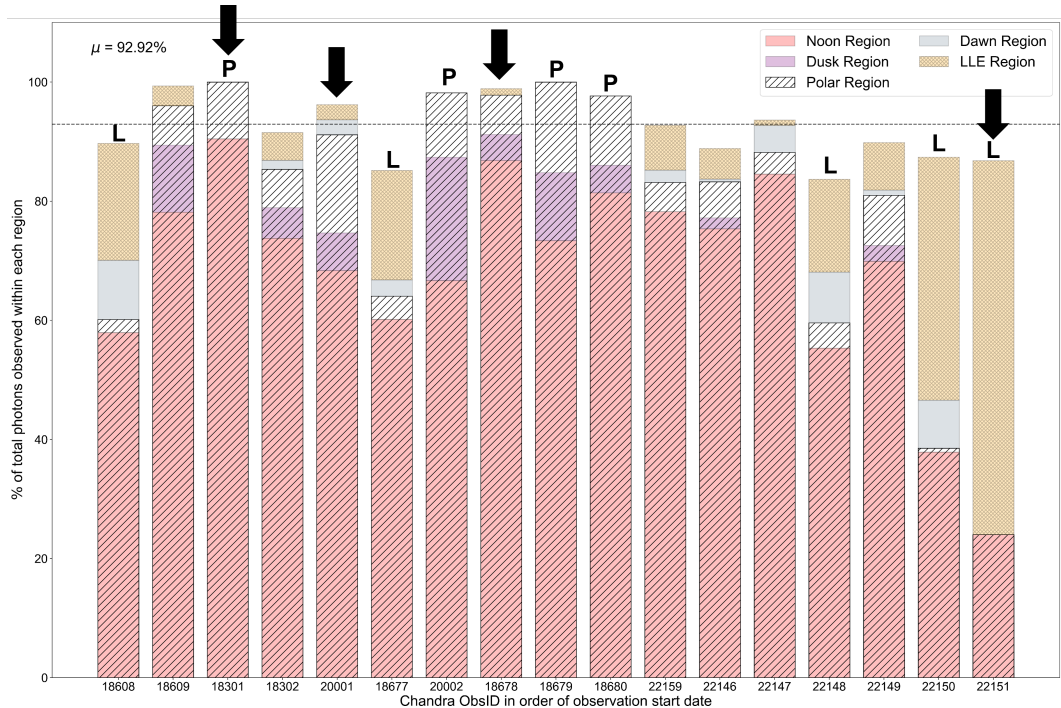


Figure 3. Stacked bar chart showing the distribution of all concentrated X-ray auroral emissions in each structure across the Juno-era Chandra observations (in order of date: Table 1), within the CML range. Each structure in both panels are labelled with identical colouring used in Figure 1. The mean, μ , is given and indicated by the horizontal line. The letters ‘P’ and ‘L’ above the bars indicate auroral morphologies that fall into either the ‘fully polar emissions’ or ‘low latitude emissions’ categories respectively, as defined in the text. The examples shown in Figure 1 are highlighted by black arrows.

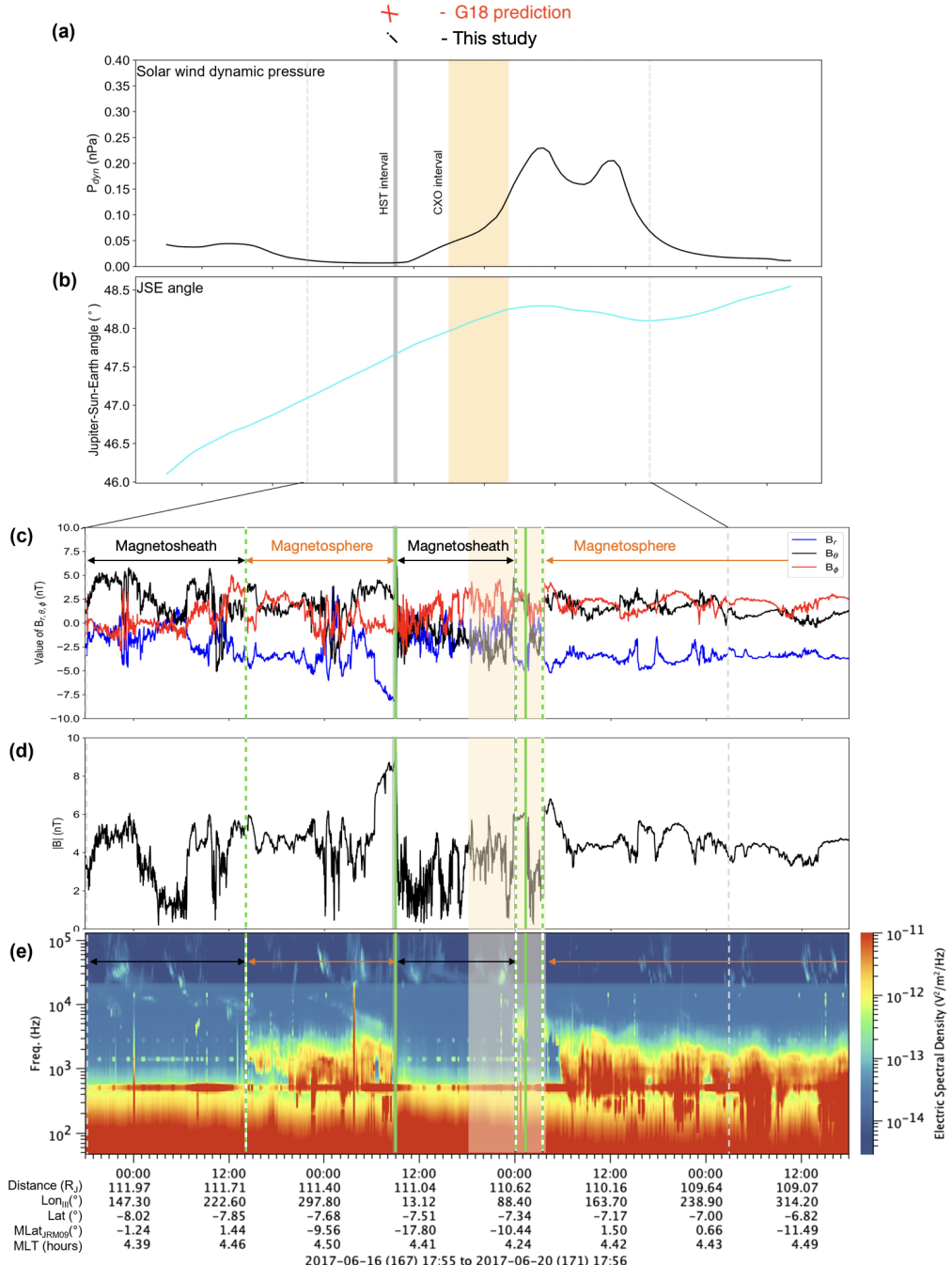
18609, 18678, 22149) and an additional smaller population at X-ray dawn (20001, 18302, 22159) highlight possible elongation of the auroral emissions in both poleward and equatorward directions and/or possible X-ray emissions associated with UV injections.

From Figure 3, we can pick out two categories: (1) fully polar emissions (i.e. X-ray polar population $\geq 95\%$ of all auroral emissions) and (2) low latitude emissions (i.e. LLE photon population $> 10\%$). These observations are labelled with ‘P’ and ‘L’ for both categories respectively. The observations that exhibit intermediate behaviour between both categories (i.e. no ‘P’ or ‘L’ label) may imply a time-dependent relationship and therefore a link between the two. We do however need to compare the mapping of these morphologies with HST and Juno data to verify such a state. The key result we present here is the lack of uniformity across Figure 3 which shows that different regions can dominate when observing the northern concentrated X-ray auroral emissions. Adding a magnetospheric context this may suggest either that: (i) the switching on/off of potential magnetospheric drivers is likely to dominate or (ii) the regions where conditions are right for wave growth (i.e. standing Alfvén waves and/or EMIC waves on the magnetopause boundary) is changing. This is emphasized in Figure S3 (in SI) which shows scatter plots of photons observed in the polar region versus the LLE region and both regions plotted against inferred solar wind conditions from the Tao et al. (2005) model. As reflected in Figure 3, we observe an anticorrelation between photons population the polar and LLE regions. There is no clear link between solar wind dynamic pressure and these populations. This may indicate that either disturbances from the solar wind are observed in multiple regions and/or the LLE region ‘switching on’ is not directly linked to the compression and may lag ahead/behind the disturbance (i.e. similar to i/I -family). Further exploration into this is beyond the scope of this work although we hope our results will highlight key examples to use in future case studies.

3.3 Using *in situ* and remote sensing diagnostics to infer magnetospheric state

In order to understand the state of the jovian magnetosphere during the Chandra interval and constrain the driver(s) responsible for variable X-ray aurora, we combine predicted solar wind conditions from the 1D MHD propagation model by Tao et al. (2005) with data from the Juno fluxgate magnetometer (Juno MAG) and the radio and plasma wave instrument (Juno Waves). The purpose of the model is to infer how solar wind conditions can cause the jovian magnetosphere to contract and/or expand. We can therefore infer the state of the jovian magnetosphere, within an error of 2 days centred on the Chandra observation based on the alignment of the Sun, Earth and Jupiter. We also compare the predicted UV auroral families during the interval to the Juno data to verify the auroral behaviour and morphology. The aim here is to combine the UV and X-ray predicted morphologies with observed solar wind conditions as a possible proxy for magnetospheric conditions when there is no upstream *in situ* data.

Figure 4 shows the results of the Tao et al. (2005) 1D MHD solar wind propagation model combined with Juno MAG and Waves data, covering 4 days centred on the Chandra (CXO) observation (shaded in orange) taken on 16 June 2017 (ObsID 20001 - see Table 1 and Figure 1c)). The propagation model predicted many intervals where the solar wind dynamic pressure (P_{dyn}) was increased when acting on the jovian magnetosphere within model error, during a relatively reasonable Jupiter-Sun-Earth (JSE) alignment (panels (a) and (b)). We only consider JSE angles $< |60^\circ|$ (highlighted in cyan) to ensure that the errors of the model are within the 2 day window, centered on the CXO interval. This conservative angle range allows us to explore of the Chandra catalogue, and compare how the model performs with real *in situ* data. The HST observation is shown by the gray interval. Both CXO and HST observations lie within the 2 day window accounting for errors in the Tao et al. (2005) model (gray dashed lines). This example was selected as this Chandra interval and Juno particle data were previously anal-



(Caption on next page)

Figure 4. Multi-panelled plot combining the results from the Tao et al. (2005) 1D MHD solar wind propagation model with Juno MAG and Waves, covering 4 days centring the Chandra observation (orange area) taken on 16 June 2017 (ObsID 20001 - see Table 1 for more details). Panels (a) and (b) show the predicted solar wind dynamic pressure (P_{dyn}) and associated JSE angle respectively, evolving over time with the Chandra (CXO) and HST observing intervals (gray area) shown in all panels. The angle represented in cyan shows periods of time when the value is $< |60^\circ|$. Panels (c) and (d) show the Juno MAG in spherical components (B_r : blue, B_θ : black, B_ϕ : red) and the total field strength ($|B|$) measured by the Juno MAG data, in units of nanotesla (nT), within the Tao uncertainty window used in our analysis. (dashed gray vertical lines: shown in all panels). Panel (e) shows the concurrent Juno Waves data, measuring the electric spectral density of the radio and plasma wave emissions. The Juno ephemeris data during this interval is displayed at the bottom, showing its position in Jupiter's System III frame (in radial distance from Jupiter, R_J , and magnetic local time (MLT; hours)) and its position projected onto Jupiter's surface (SIII lon (Lon_{III}; degrees), SIII lat (Lat; degrees) and magnetic latitude found from the JRM09 field model (MLat_{JRM09}; degrees)). The green-white dashed and solid green vertical lines represent Juno making inbound and outbound crossings of the magnetopause boundary respectively, as identified from Juno JADE data as described in Weigt et al. (2020). Juno's known position in the magnetosheath (black arrows) and magnetosphere (orange arrows) are also labelled. The identified UV auroral family using the Grodent et al. (2018) definitions from G18 (red) and this study (black), as shown in Table 1, are at the top of panel (a).

447 ysed by Weigt et al. (2020) to identify magnetopause crossings to infer a dynamic pres-
 448 sure from the Joy et al. (2002) model. When compared to the distributions of solar wind
 449 dynamic pressure (P_{dyn}) identified by Jackman and Arridge (2011) from upstream so-
 450 lar wind data at Jupiter spanning 1973 to 2004, both the Tao model and Juno data find
 451 the jovian magnetosphere to be compressed during this time ($P_{\text{dyn}} = \sim 0.23 - 0.39$ nPa).
 452 These values lie at the upper tail of the distribution where the typical P_{dyn} observed from
 453 spacecraft data was 0.04 nPa.

454 The magnetopause crossings identified by Weigt et al. (2020) from Juno JADE data
 455 (green-white dashed and green solid vertical lines represent Juno making inbound and
 456 outbound respectively) are confirmed in the other Juno datasets (as shown in panels (c)
 457 - (e)) with a sharp change in the total magnetic field strength ($|B|$), in units of nanotesla
 458 (nT), and its spherical components (B_r : blue, B_θ : black, B_ϕ : red). The character of the
 459 magnetic field also changes during a crossing as it is noisier in the magnetosheath than
 460 in the magnetosphere. To locate the magnetopause boundary crossings (labelled with
 461 orange and black arrows), one can look at the Waves data (panel (e); colour bar show-
 462 ing the electric spectral density of the radio emissions), and in particular the appearance/disappearance
 463 of the non-thermal trapped continuum emissions (as conducted by Hospodarsky et al.
 464 (2017)). These emissions, observed between the electron plasma frequency and ~ 10 kHz,
 465 located in the jovian magnetospheric cavity where the emission frequency exceeds that
 466 of the surrounding plasma frequency (e.g., Gurnett and Scarf (1983)). When in the mag-
 467 netosheath, the trapped continuum emissions are blocked by the denser sheath plasma.
 468 These emissions appear again when Juno enters the more rarefied magnetospheric plasma.
 469 These transitions in electric spectral density also align with the identified Juno cross-
 470 ings.

471 Finally, during the series of compressions Grodent et al. (2018) found that the UV
 472 auroral emissions exhibited features associated with the *X*-family (red label above panel
 473 (a)), suggesting that the magnetosphere was being affected by a solar wind compression

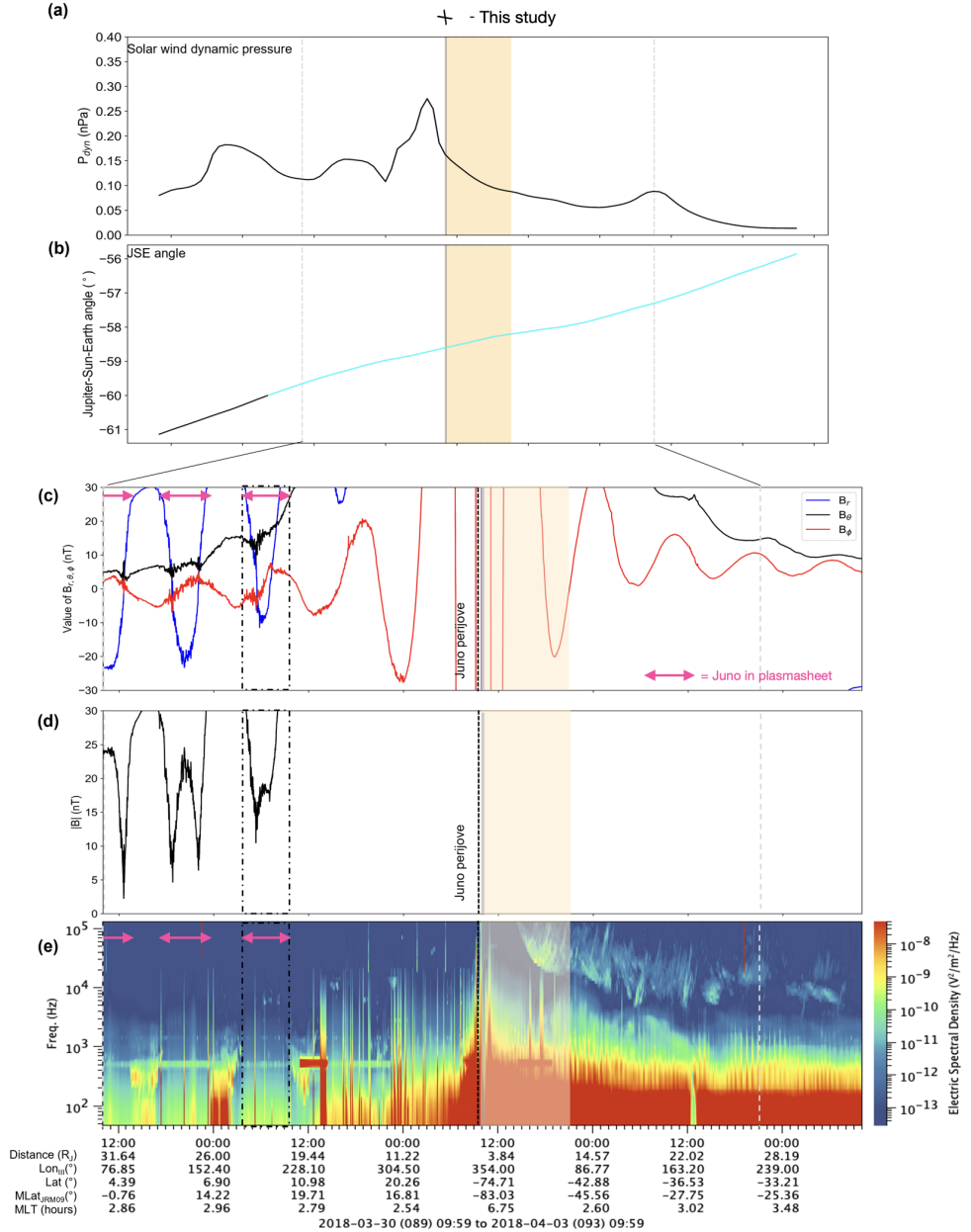


Figure 5. Multi-panel plot for ObsID 18678 (1 April 2018) in identical format to Figure 4. The interval of the Juno perijove is shown by the black dashed line. Dotted black box highlights interval of potential dipolarization of the magnetic field (mainly in B_θ) associated with possible injection events in the UV aurora. The Grodent et al. (2018) UV family identified in this study is shown at the top of panel (a). Intervals when Juno is in the plumesheet, identified from Juno Waves, prior to perijove are shown with pink arrows.

region. When comparing these results to Figure 3, the X-ray auroral emissions spans across multiple regions and are dominated by X-ray noon. We identify this morphology to likely be associated with the *i*-family (black label) or moderate injections which often occur after an external perturbation [see G18]. The X-ray morphology is observed to be between our defined categories and agree with Weigt et al. (2020) who observe the northern auroral emissions to be more extended and map to the dayside magnetopause boundary, along the noon-dusk sector using the Vogt et al. (2011, 2015) flux equivalence model. This may therefore suggest that, in this case, the auroral morphology reflects a magnetosphere disturbed in multiple regions and the the emissions likely remain poleward and more concentrated during intervals of compressions. This example was used as a “proof of concept” of compression identification as the location of Juno was near its apojoove position. This allows analysis of the magnetospheric response to changing solar wind conditions in the *in situ* data.

Figure 5 shows an example when Juno is near perijove during the Chandra interval on 1 April 2018 (ObsID 18678 - see Table 1 and Figure 1d)), making it difficult to infer the state of the magnetosphere due to the very strong field strength as you approach Jupiter (panels (c) and (d)). Juno made several plasmashell crossings prior to the CXO interval as shown by the sharp transition in electric spectral density, where the denser plasmashell blocks the continuum emissions via refraction effects (analogous to the case of magnetopause crossings). Intervals when Juno is inside the plasmashell are indicated by pink arrows. From this position we have limited ability from the *in situ* measurements to infer the upstream conditions, unlike at apojoove when magnetopause boundary crossings can give us snapshots of magnetospheric size and inferred upstream dynamic pressure.

As shown in panels (a) and (b), the Tao et al. (2005) model suggests that there is a series of solar wind compressions during the Juno perijove interval, with maximum pressure of 0.275 nPa. In our analysis we identify that the UV auroral morphology was associated with the *X*-family, agreeing with the predicted model results, coinciding with the start of the CXO interval. As shown in panel (e), the spectrogram contains a variety of identifiable features including: periodic emissions (up to ~ 1 - 100 kHz as bursts of high electric spectral density); broadband kilometric (bKOM) emissions in highest frequency channels, notably after perijove and the aforementioned continuum emissions, used as indicator of plasmashell crossings. Therefore it is difficult to disentangle sources associated with the state of the jovian magnetosphere and verify the model results. We do however highlight a region of potential activity, as the dotted black box in Figure 5, in the magnetic field associated with a possible dipolarization of the field when Juno is inside the plasmashell. A dipolarization occurs when the magnetic field line which Juno travels across changes from a stretched to a more dipolar configuration after a tail reconnection event, producing an anomalous feature in the B_θ component. Such dipolarizations of the field have been found to be associated with injection events found from HST UV observations and can be accompanied by bright dawn storm emissions (Yao et al., 2020). These bright dawn storm emissions have been found to be correlated with a brightening of HXR intensity in the jovian aurora (Wibisono et al., 2021), likely linked to similar regions of electron bremsstrahlung activity (e.g., Branduardi-Raymont et al. (2008)). We do note that as the CXO interval was 2-3 jovian rotations after the potential injection event, it is unlikely that the X-ray morphology will reflect this behaviour. However, with the identified *X*-family (and its links to moderate injections) in the UV emissions the magnetosphere, across many sectors during this interval, is likely to be in a disturbed state.

When comparing Figure 5 to Figure 3, the auroral emissions found in ObsID 18678 exhibited morphology in between our defined categories. Like majority of emissions located in the X-ray polar region with a small portion of the emissions located in the LLE region (< 10%). The small population of X-ray dusk photons indicate that the morphol-

ogy extended polewards similar to ObsID 20001. Comparing Figures 1c) and (d), the auroral morphology is very similar with the exception of the dawn region. Therefore this distribution of X-ray auroral photons and UV auroral behaviour may be an indicator of a disturbed magnetosphere due to a potential compression event. Identifying such disturbances may be associated with a possible injection event which may precede or follow a compression event as observed by G18. We do note that further in depth analysis of the magnetic field and particle data is needed to confirm this, however the results provided here will likely highlight this observation (and many others associated with possible disturbances) as one of interest for further study.

536 4 Summary and Discussion

537 We present X-ray ‘auroral structures’ mapping to various regions in the magnetosphere linking X-ray auroral morphology to magnetospheric dynamics in the jovian system. Using CXO, HST and Juno data spanning the majority of Juno’s main mission (24
538 May 2016 to 8 September 2019), we are able to compare observed magnetospheric dy-
539 namics to UV and X-ray remote sensing data. The results of our auroral distributions
540 can be summarised as follows:

- 543 1. The X-ray auroral emissions show two clear categories of auroral morphological
544 distributions: (1) fully polar aurora (2) low latitude emissions.
- 545 2. Non-uniformity of auroral distributions suggest there are likely numerous drivers
546 responsible for the X-ray northern auroral emissions or conditions in the magne-
547 tosphere that permit the growth of drivers (i.e. EMIC waves) change.
- 548 3. Using UV and X-ray morphologies together may be a useful proxy for solar wind
549 conditions (particularly during compressions) to identify magnetospheric distur-
550 bances.
- 551 4. Visibility (or planetary tilt) has very little effect when observing the auroral pho-
552 ton distributions.
- 553 5. X-ray auroral distributions may highlight potential magnetospheric phenomena
554 (i.e., prior injection events) for future study.

555 We note that only CXO observations which had a HST observation ± 1 day from
556 the Chandra window were considered for this study. For example, ObsID 20002 (6 Au-
557 gust 2017; see full catalogue in Weigt, Jackman, et al. (2021)) does not appear in our
558 study, however initial analysis of magnetopause crossings made by Juno suggest that the
559 magnetosphere was compressed during this time using the Joy et al. (2002) model.

560 From the non-uniformity across the northern auroral distributions (Figure 3) and
561 our visibility modelling of the regions, the lack of emissions we observe in a given region
562 is more likely associated with the switching on/off of drivers. The X-ray noon popula-
563 tion dominates the majority of observations suggesting that the likely driver from these
564 emissions lies on the noon magnetopause boundary, as observed by Weigt, Jackman, et
565 al. (2021). Here, X-ray noon coincides with the location of the UV polar and swirl re-
566 gion and therefore linked to a very dynamic region of the dayside magnetosphere. Day-
567 side drivers such as magnetic reconnection would occur more frequently on the noon mag-
568 netosphere compared to other regions, especially during periods of high P_{dyn} . In these
569 situations the solar wind is likely to reconnect with the jovian outer magnetosphere ei-
570 ther at high latitudes in the cusps (Bunce et al., 2004) or compressions may induce re-
571 connection inside the jovian system (i.e., at multiple smaller sites in the plasmashell with
572 more drizzle-like reconnection (Guo et al., 2018)). We note that previous analysis of three
573 intervals during compression events (ObsID 20001, 20002, 18678) were found to exhibit
574 very significant quasi-periodic oscillations (QPOs) within a region located in the center
575 of X-ray noon (the averaged hot spot nucleus (AHSNuc)). These QPOs were observed
576 to be between 2- and 4- minutes suggesting very dynamic activity on the noon bound-

577 ary and timescales linked to magnetic reconnection on the boundary (Weigt, Jackman,
 578 et al., 2021). However, Weigt, Jackman, et al. (2021) observed that time QPOs were likely
 579 to be spatial dependent and therefore the period and statistical significance changes with
 580 where you observe in the aurora. They also stated that any activity may be initiated at
 581 the noon magnetopause boundary and be advected along the magnetopause boundary
 582 towards the flanks. This may explain the non-uniformity of auroral distributions we dis-
 583 cuss here and how wave growth is promoted in other regions of the magnetosphere such
 584 as the strong correlations between X-ray emissions and EMIC waves found in the outer
 585 dawn and midnight magnetosphere (Yao et al., 2021). Therefore, assuming the auroral
 586 emissions are generated from wave activity, the changing auroral morphology may re-
 587 veal the propensity for wave activity in different components in the jovian magnetosphere.

588 The peak visibility of each X-ray auroral structure was within our CML threshold
 589 throughout the Juno era during with changing sub-Earth latitudes mainly affecting those
 590 regions nearest to the pole (i.e., X-ray dusk). We do note however that the changing sub-
 591 Earth latitudes will have the greatest effect in the southern auroral region. Therefore
 592 future studies will need to develop a new set of X-ray auroral structures to combat this
 593 effect. The techniques discussed in this study can be extended to the southern auroral
 594 region and will allow detailed exploration and comparisons between both auroral regions
 595 (i.e., North-South asymmetry and non-conjugacy observed in the auroral X-ray emis-
 596 sions Branduardi-Raymont et al. (2004); Jackman et al. (2018); Weigt, Jackman, et al.
 597 (2021); Mori et al. (2022) and other wavelengths). This has already been shown by Mori
 598 et al. (2022) for HXRs, where non-thermal bremsstrahlung X-rays were \sim twice as bright
 599 in the southern auroral region than the North, consistent with more persistent and stronger
 600 electron currents than those observed in the North (Kotsiaros et al., 2019).

601 In order to fully categorise the jovian X-ray auroral emissions and the extent of the
 602 solar wind influence at both poles, current X-ray technology needs to be expanded upon.
 603 Future potential missions such as Lynx (Falcone et al., 2019) and Line Emission Map-
 604 per (LEM; Kraft et al. (2022)) will allow us to explore in detail the various drivers gen-
 605 erating X-ray emissions in the jovian magnetosphere. Utilising the enhanced spectral res-
 606 olution i.e., 1-2 eV spectral resolution in the 0.2-2 keV range for LEM) and greater ef-
 607 fective area at lower energies, we will be able to delve into the softer X-ray spectrum and
 608 evaluate the ion populations dominating various X-ray processes (e.g., charge exchange)
 609 and eventually including the southern hemisphere. Coupling these remote sensing instru-
 610 ments with data from an *in situ* X-ray probe (Dunn et al., 2023) will be the key to fully
 611 understanding the magnetospheric drivers responsible for the jovian auroral X-ray emis-
 612 sions.

613 Data Availability Statement

614 This research has made use of data obtained from the *Chandra Data Archive* and
 615 *Chandra Source Catalogue* (<https://cda.harvard.edu/chaser/>); Juno Waves and MAG
 616 from the *NASA Planetary Data System* and solar wind data obtained via AMDA
 617 (<http://amda.cdpp.eu/>). Waves survey data are at <https://doi.org/10.17189/1520498>
 618 . The catalogue of Chandra data required to reproduce the results shown in this study
 619 are stored in the Zenodo repository at <http://doi.org/10.5281/zenodo.4275744>.

620 Acknowledgments

621 DMW is supported by the Science and Technology Facilities Council (STFC) studentship
 622 ST/S505705/1 and long term attachment grant to work at the Dublin Institute for Ad-
 623 vanced Studies (DIAS). DMW's work at DIAS is funded by European Union's Horizon
 624 2020 research and innovation programme under grant agreement No. 952439 and project
 625 number AO 2-1927/22/NL/GLC/ov as part of the ESA OSIP Nanosats for Spaceweather
 626 Campaign. DMW's work at Trinity College Dublin is supported by Air Force Office of

627 Scientific Research award FA9550-19-1-7010. DMP is supported by a LUFST studentship.
 628 SVB is supported by STFC projects ST/M005534/1 and ST/V000748/1. CMJ, CKL and
 629 SCMcE work at DIAS is supported by the Science Foundation Ireland (SFI) Grant 18/FRL/6199.
 630 WRD was supported by Ernest Rutherford Fellowship: ST/W003449/1. CT acknowl-
 631 edges support by JSPS KAKENHI 20KK0074. The research at the University of Iowa
 632 is supported by NASA through Contract 699041X with Southwest Research Institute.

633 References

- 634 Badman, S. V., Branduardi-Raymont, G., Galand, M., Hess, S. L. G., Krupp, N.,
 635 Lamy, L., ... Tao, C. (2015). Auroral Processes at the Giant Planets: Energy
 636 Deposition, Emission Mechanisms, Morphology and Spectra. *Space Science Re-
 637 views*, 187(1-4), 99–179. Retrieved from <http://dx.doi.org/10.1007/s11214-014-0042-x> doi:
 638 10.1007/s11214-014-0042-x
- 640 Bolton, S. J., Lunine, J., Stevenson, D., Connerney, J. E. P., Levin, S., Owen,
 641 T. C., ... Thorpe, R. (2017). The Juno Mission. *Space Science Reviews*,
 642 213(1-4), 5–37. Retrieved from <http://dx.doi.org/10.1007/s11214-017-0429-6> doi:
 643 10.1007/s11214-017-0429-6
- 645 Bonfond, B., Saur, J., Grodent, D., Badman, S. V., Bisikalo, D., Shematovich, V.,
 646 ... Radioti, A. (2017). The tails of the satellite auroral footprints at Jupiter.
 647 *Journal of Geophysical Research (Space Physics)*, 122(8), 7985–7996. doi:
 648 10.1002/2017JA024370
- 649 Bonfond, B., Yao, Z. H., Gladstone, G. R., Grodent, D., Gérard, J., Matar, J., ...
 650 Bolton, S. J. (2021). Are Dawn Storms Jupiter's Auroral Substorms? *AGU
 651 Advances*, 2(1), 1–14. doi: 10.1029/2020av000275
- 652 Branduardi-Raymont, G., Elsner, R. F., Galand, M., Grodent, D., Cravens, T. E.,
 653 Ford, P., ... Waite, J. H. (2008). Spectral morphology of the X-ray emis-
 654 sion from Jupiter's aurorae. *Journal of Geophysical Research: Space Physics*,
 655 113(2), 1–11. doi: 10.1029/2007JA012600
- 656 Branduardi-Raymont, G., Elsner, R. F., Gladstone, G. R., Ramsay, G., Rodriguez,
 657 P., Soria, R., & Waite, J. H. (2004). First observation of Jupiter by XMM-
 658 Newton. *Astronomy*, 337(1149), 331–337. doi: 10.1051/0004-6361
- 659 Bunce, E. J., Cowley, S. W., & Yeoman, T. K. (2004). Jovian cusp processes: Impli-
 660 cations for the polar aurora. *Journal of Geophysical Research: Space Physics*,
 661 109(A9), 1–26. doi: 10.1029/2003JA010280
- 662 Connerney, J. E. P., Benn, M., Bjarno, J. B., Denver, T., Espley, J., Jorgensen,
 663 J. L., ... Smith, E. J. (2017). The Juno Magnetic Field Investigation. *Space
 664 Science Reviews*, 213(1-4), 39–138. Retrieved from [http://dx.doi.org/
 665 10.1007/s11214-017-0334-z](http://dx.doi.org/10.1007/s11214-017-0334-z) doi: 10.1007/s11214-017-0334-z
- 666 Dumont, M., Grodent, D., Radioti, A., Bonfond, B., & Gérard, J. (2014). Jupiter's
 667 equatorward auroral features: Possible signatures of magnetospheric injec-
 668 tions. *Journal of Geophysical Research: Space Physics*, 119(12), A07000.
 669 Retrieved from [http://doi.wiley.com/10.1029/2006JA011892https://
 671 onlinelibrary.wiley.com/doi/abs/10.1002/2014JA020527](http://doi.wiley.com/10.1029/2006JA011892https://

 670 onlinelibrary.wiley.com/doi/abs/10.1002/2014JA020527) doi:
 672 10.1002/2014JA020527
- 673 Dumont, M., Grodent, D., Radioti, A., Bonfond, B., Roussos, E., & Paranicas,
 674 C. (2018). Evolution of the Auroral Signatures of Jupiter's Magnetospheric
 675 Injections. *Journal of Geophysical Research: Space Physics*, 123(2015), 1–
 676 13. Retrieved from <http://doi.wiley.com/10.1029/2018JA025708> doi:
 677 10.1029/2018JA025708
- 678 Dunn, W., Berland, G., Roussos, E., Clark, G., Kollmann, P., Turner, D., ... Kraft,
 679 R. P. (2023, March). Exploring Fundamental Particle Acceleration and Loss
 Processes in Heliophysics through an Orbiting X-ray Instrument in the Jovian

- 680 System. *arXiv e-prints*, arXiv:2303.02161. doi: 10.48550/arXiv.2303.02161
- 681 Dunn, W. R. (2022). X-Ray Emissions from the Jovian System. In *Handbook of x-*
 682 *ray and gamma-ray astrophysics*. edited by cosimo bambi and andrea santangelo
 683 (p. 110). doi: 10.1007/978-981-16-4544-0_73-1
- 684 Dunn, W. R., Branduardi-Raymont, G., Elsner, R. F., Vogt, M. F., Lamy, L., Ford,
 685 P. G., ... Jasinski, J. M. (2016). The impact of an ICME on the Jovian X-ray
 686 aurora. *Journal of Geophysical Research A: Space Physics*, *121*(3), 2274–2307.
 687 doi: 10.1002/2015JA021888
- 688 Dunn, W. R., Branduardi-Raymont, G., Ray, L. C., Jackman, C. M., Kraft, R. P.,
 689 Elsner, R. F., ... Coates, A. J. (2017). The independent pulsations of Jupiter's
 690 northern and southern X-ray auroras. *Nature Astronomy*, *1*(11), 758–764.
 691 Retrieved from <http://dx.doi.org/10.1038/s41550-017-0262-6> doi:
 692 10.1038/s41550-017-0262-6
- 693 Dunn, W. R., Branduardi-Raymont, G., Carter-Cortez, V., Campbell, A., Elsner,
 694 R., Ness, J.-U., ... Achilleos, N. (2020). Jupiter's X-ray Emission During the
 695 2007 Solar Minimum. *Journal of Geophysical Research: Space Physics*, *125*(6),
 696 e2019JA027219. Retrieved from <https://onlinelibrary.wiley.com/doi/abs/10.1029/2019JA027219> doi: 10.1029/2019JA027219
- 697 Dunn, W. R., Gray, R., Wibisono, A. D., Lamy, L., Louis, C., Badman, S. V., ...
 698 Kraft, R. (2020). Comparisons Between Jupiter's X-ray, UV and Radio
 699 Emissions and In-Situ Solar Wind Measurements During 2007. *Journal of*
 700 *Geophysical Research: Space Physics*, *125*(6), e2019JA027222. Retrieved from
 701 <https://onlinelibrary.wiley.com/doi/abs/10.1029/2019JA027222> doi:
 702 10.1029/2019JA027222
- 703 Dunn, W. R., Weigt, D. M., Grodent, D., Yao, Z. H., May, D., Feigelman, K., ...
 704 Ray, L. C. (2022). Jupiter's X-ray and UV Dark Polar Region. *Geophysical*
 705 *Research Letters*, *4*. Retrieved from <https://onlinelibrary.wiley.com/doi/10.1029/2021GL097390> doi: 10.1029/2021GL097390
- 706 Elsner, R. F., Lugaz, N., Waite, J. H., Cravens, T. E., Gladstone, G. R., Ford, P.,
 707 ... Majeed, T. (2005). Simultaneous Chandra X ray Hubble Space Telescope
 708 ultraviolet, and Ulysses radio observations of Jupiter's aurora. *Journal of Geo-*
 709 *physical Research: Space Physics*, *110*(A1), 1–16. doi: 10.1029/2004JA010717
- 710 Falcone, A. D., Kraft, R. P., Bautz, M. W., Gaskin, J. A., Mulqueen, J. A., &
 711 Swartz, D. A. (2019). Overview of the high-definition x-ray imager instrument
 712 on the Lynx x-ray surveyor. *Journal of Astronomical Telescopes, Instruments,*
 713 *and Systems*, *5*(2). doi: 10.1111/1.JATIS.5.2.021019
- 714 Gerard, J. C., Grodent, D., Prange, R., Waite, J. H., Gladstone, G. R., Dols, V., ...
 715 Franke, K. A. (1994). A Remarkable Auroral Event on Jupiter Observed in the
 716 Ultraviolet with the Hubble Space Telescope. *Science*, *266*(5191), 1675–1678.
 717 doi: 10.1126/science.266.5191.1675
- 718 Gray, R. L., Badman, S. V., Bonfond, B., Kimura, T., Misawa, H., Nichols, J. D.,
 719 ... Ray, L. C. (2016). Auroral evidence of radial transport at Jupiter during
 720 January 2014. *Journal of Geophysical Research: Space Physics*, *121*(10), 9972–
 721 9984. Retrieved from <https://onlinelibrary.wiley.com/doi/abs/10.1002/2016JA023007> doi: 10.1002/2016JA023007
- 722 Greathouse, T., Gladstone, R., Versteeg, M., Hue, V., Kammer, J., Giles, R., ...
 723 Vogt, M. F. (2021). Local Time Dependence of Jupiter's Polar Auroral Emis-
 724 sions Observed by Juno UVS. *Journal of Geophysical Research: Planets*,
 725 *126*(12), 1–13. doi: 10.1029/2021JE006954
- 726 Grodent, D. (2015). A Brief Review of Ultraviolet Auroral Emissions on Giant Plan-
 727 etes. *Space Science Reviews*, *187*(1-4), 23–50. Retrieved from <http://dx.doi.org/10.1007/s11214-014-0052-8> doi: 10.1007/s11214-014-0052-8
- 728 Grodent, D., Bonfond, B., Yao, Z., Gérard, J. C., Radioti, A., Dumont, M., ...
 729 Valek, P. (2018). Jupiter's Aurora Observed With HST During Juno Orbits 3
 730 to 7. *Journal of Geophysical Research: Space Physics*, *123*(5), 3299–3319. doi:
 731 10.1029/2017JA027222

- 735 10.1002/2017JA025046
- 736 Grodent, D., Clarke, J. T., Kim, J., Waite, J. H., & Cowley, S. W. H. (2003).
 737 Jupiter's main auroral oval observed with HST-STIS. *Journal of Geophysical*
 738 *Research (Space Physics)*, 108(A11), 1389. doi: 10.1029/2003JA009921
- 739 Grodent, D., Clarke, J. T., Waite, J. H., Cowley, S. W., Gérard, J. C., & Kim, J.
 740 (2003). Jupiter's polar auroral emissions. *Journal of Geophysical Research: Space*
 741 *Physics*, 108(A10), 1–9. doi: 10.1029/2003JA010017
- 742 Guo, R. L., Yao, Z. H., Sergis, N., Wei, Y., Mitchell, D., Roussos, E., ... Wan,
 743 W. X. (2018). Reconnection Acceleration in Saturn's Dayside Magnetodisk:
 744 A Multicase Study with Cassini. *The Astrophysical Journal*, 868(2), L23.
 745 Retrieved from <http://dx.doi.org/10.3847/2041-8213/aaedab> doi:
 746 10.3847/2041-8213/aaedab
- 747 Gurnett, D. A., & Scarf, F. L. (1983). Plasma waves in the jovian magnetosphere.
 748 In A. J. Dessler (Ed.), *Physics of the jovian magnetosphere* (p. 285–316). Cambridge University Press. doi: 10.1017/CBO9780511564574.010
- 749 Hospodarsky, G. B., Kurth, W. S., Bolton, S. J., Allegrini, F., Clark, G. B., Connerney, J. E., ... Valek, P. W. (2017). Jovian bow shock and magnetopause encounters by the Juno spacecraft. *Geophysical Research Letters*, 44(10), 4506–4512. doi: 10.1002/2017GL073177
- 750 Houston, S. J., Cravens, T. E., Schultz, D. R., Gharibnejad, H., Dunn, W. R., Haggerty, D. K., ... Ozak, N. (2020). Jovian Auroral Ion Precipitation: X-Ray Production From Oxygen and Sulfur Precipitation. *Journal of Geophysical Research: Space Physics*, 125(2), 2019JA027007. Retrieved from <https://onlinelibrary.wiley.com/doi/10.1029/2019JA027007> doi: 10.1029/2019JA027007
- 751 Jackman, C. M., & Arridge, C. S. (2011). Solar Cycle Effects on the Dynamics of Jupiter's and Saturn's Magnetospheres. *Solar Physics*, 274(1-2), 481–502. doi: 10.1007/s11207-011-9748-z
- 752 Jackman, C. M., Knigge, C., Altamirano, D., Gladstone, R., Dunn, W., Elsner, R., ... Ford, P. (2018). Assessing Quasi-Periodicities in Jovian X-Ray Emissions: Techniques and Heritage Survey. *Journal of Geophysical Research: Space Physics*, 123(11), 9204–9221. doi: 10.1029/2018JA025490
- 753 Joy, S. P., Kivelson, M. G., Walker, R. J., Khurana, K. K., Russell, C. T., & Ogino, T. (2002). Probabilistic models of the Jovian magnetopause and bow shock locations. *Journal of Geophysical Research: Space Physics*, 107(A10), 1–17. doi: 10.1029/2001JA009146
- 754 Kimura, T., Nichols, J. D., Gray, R. L., Tao, C., Murakami, G., Yamazaki, A., ... Fujimoto, M. (2017). Transient brightening of Jupiter's aurora observed by the Hisaki satellite and Hubble Space Telescope during approach phase of the Juno spacecraft. *Geophysical Research Letters*, 44(10), 4523–4531. doi: 10.1002/2017GL072912
- 755 Kotsiaros, S., Connerney, J. E., Clark, G., Allegrini, F., Gladstone, G. R., Kurth, W. S., ... Levin, S. M. (2019). Birkeland currents in Jupiter's magnetosphere observed by the polar-orbiting Juno spacecraft. *Nature Astronomy*, 3(10), 904–909. Retrieved from <http://dx.doi.org/10.1038/s41550-019-0819-7> doi: 10.1038/s41550-019-0819-7
- 756 Kraft, R., Markevitch, M., Kilbourne, C., Adams, J. S., Akamatsu, H., Ayromlou, M., ... ZuHone, J. (2022, November). Line Emission Mapper (LEM): Probing the physics of cosmic ecosystems. *arXiv e-prints*, arXiv:2211.09827. doi: 10.48550/arXiv.2211.09827
- 757 Kurth, W. S., Hospodarsky, G. B., Kirchner, D. L., Mokrzycki, B. T., Averkamp, T. F., Robison, W. T., ... Zarka, P. (2017). The Juno Waves Investigation. *Space Science Reviews*, 213(1-4), 347–392. Retrieved from <http://dx.doi.org/10.1007/s11214-017-0396-y> doi: 10.1007/s11214-017-0396-y
- 758 Louarn, P., Paranicas, C. P., & Kurth, W. S. (2014). Global magnetodisk distur-

- bances and energetic particle injections at Jupiter. *Journal of Geophysical Research: Space Physics*, 119(6), 4495–4511. doi: 10.1002/2014JA019846
- McComas, D. J., Szalay, J. R., Allegrini, F., Bagenal, F., Connerney, J., Ebert, R. W., ... Bolton, S. (2017). Plasma environment at the dawn flank of Jupiter's magnetosphere: Juno arrives at Jupiter. *Geophysical Research Letters*, 44(10), 4432–4438. doi: 10.1002/2017GL072831
- McEntee, S. C., Jackman, C. M., Weigt, D. M., Dunn, W. R., Kashyap, V., Kraft, R., ... Gallagher, P. T. (2022). Comparing jupiter's equatorial x-ray emissions with solar x-ray flux over 19 years of the chandra mission. *Journal of Geophysical Research: Space Physics*, 127. Retrieved from <https://onlinelibrary.wiley.com/doi/10.1029/2022JA030971> doi: 10.1029/2022JA030971
- Mori, K., Hailey, C., Bridges, G., Mandel, S., Garvin, A., Grefenstette, B., ... Ray, L. (2022). Observation and origin of non-thermal hard X-rays from Jupiter. *Nature Astronomy*. Retrieved from <https://www.nature.com/articles/s41550-021-01594-8> doi: 10.1038/s41550-021-01594-8
- Nichols, J. D., Badman, S. V., Bagenal, F., Bolton, S. J., Bonfond, B., Bunce, E. J., ... Yoshikawa, I. (2017). Response of Jupiter's auroras to conditions in the interplanetary medium as measured by the Hubble Space Telescope and Juno. *Geophysical Research Letters*, 44(15), 7643–7652. Retrieved from <http://doi.wiley.com/10.1002/2017GL073029> doi: 10.1002/2017GL073029
- Nichols, J. D., Clarke, J. T., Gérard, J. C., Grodent, D., & Hansen, K. C. (2009). Variation of different components of jupiter's auroral emission. *Journal of Geophysical Research: Space Physics*, 114(6), 1–18. doi: 10.1029/2009JA014051
- Pallier, L., & Prangé, R. (2001). More about the structure of the high latitude Jovian aurorae. *Planetary and Space Science*, 49(10-11), 1159–1173. doi: 10.1016/S0032-0633(01)00023-X
- Swithenbank-Harris, B. G., Nichols, J. D., & Bunce, E. J. (2019). Jupiter's Dark Polar Region as Observed by the Hubble Space Telescope During the Juno Approach Phase. *Journal of Geophysical Research: Space Physics*, 124(11), 9094–9105. doi: 10.1029/2019JA027306
- Tao, C., Kataoka, R., Fukunishi, H., Takahashi, Y., & Yokoyama, T. (2005). Magnetic field variations in the Jovian magnetotail induced by solar wind dynamic pressure enhancements. *Journal of Geophysical Research: Space Physics*, 110(A11), 1–9. doi: 10.1029/2004JA010959
- Vasyliūnas, V. M. (1983). Plasma distribution and flow. In A. J. Dessler (Ed.), *Physics of the jovian magnetosphere* (pp. 395–453). Cambridge: Cambridge University Press. Retrieved from <https://www.cambridge.org/core/product/identifier/CBO9780511564574A082/type/book\part> doi: 10.1017/CBO9780511564574.013
- Vogt, M. F., Bunce, E. J., Kivelson, M. G., Khurana, K. K., Walker, R. J., Radioti, A., ... Grodent, D. (2015). Magnetosphere-ionosphere mapping at Jupiter: Quantifying the effects of using different internal field models. *Journal of Geophysical Research: Space Physics*, 120(4), 2584–2599. doi: 10.1002/2014JA020729
- Vogt, M. F., Kivelson, M. G., Khurana, K. K., Walker, R. J., Bonfond, B., Grodent, D., & Radioti, A. (2011). Improved mapping of Jupiter's auroral features to magnetospheric sources. *Journal of Geophysical Research: Space Physics*, 116(3). doi: 10.1029/2010JA016148
- Weigt, D. M., Dunn, W. R., Jackman, C. M., Kraft, R., Branduardi-Raymont, G., Nichols, J. D., ... Gladstone, G. R. (2021). Searching for Saturn's X-rays during a rare Jupiter Magnetotail crossing using Chandra. *Monthly Notices of the Royal Astronomical Society*, 506(1), 298–305. Retrieved from <https://academic.oup.com/mnras/article/506/1/298/6298248> doi:

- 845 10.1093/mnras/stab1680
 846 Weigt, D. M., Gladstone, G. R., McEntee, S. C., Dunn, W. R., Kashyap, V. L.,
 847 Jackman, C. M., ... Branduardi-Raymont, G. (2022). *Chandra-x-ray-data-processing-pipeline version 1.0.2 (v1.0.2) [computer software]*. Zenodo.
 848 doi: 10.5281/ZENODO.7380282
 849 Weigt, D. M., Jackman, C. M., Dunn, W. R., Gladstone, G. R., Vogt, M. F.,
 850 Wibisono, A. D., ... Kraft, R. P. (2020). Chandra Observations of
 851 Jupiter's X-ray Auroral Emission During Juno Apojove 2017. *Journal of Geophysical Research: Planets*, 125(4), e2019JE006262. Retrieved from
 852 <https://onlinelibrary.wiley.com/doi/abs/10.1029/2019JE006262> doi:
 853 10.1029/2019JE006262
 854 Weigt, D. M., Jackman, C. M., Vogt, M. F., Manners, H., Dunn, W. R., Gladstone,
 855 G. R., ... McEntee, S. C. (2021). Characteristics of Jupiter's X-Ray Auroral Hot Spot Emissions Using Chandra. *Journal of Geophysical Research: Space Physics*, 126(9). Retrieved from <https://onlinelibrary.wiley.com/doi/10.1029/2021JA029243> doi: 10.1029/2021JA029243
 856 Weisskopf, M. C., Tananbaum, H. D., Van Speybroeck, L. P., & O'Dell, S. L. (2000). Chandra X-ray Observatory (CXO): overview. *X-Ray Optics, Instruments, and Missions III*, 4012(July 2000), 2–16. doi: 10.1117/12.391545
 857 Wibisono, A. D., Branduardi-Raymont, G., Dunn, W. R., Kimura, T., Coates, A. J.,
 858 Grodent, D., ... Haythornthwaite, R. P. (2021). Jupiter's X-ray aurora during
 859 UV dawn storms and injections as observed by XMM-Newton, Hubble, and Hisaki. *Monthly Notices of the Royal Astronomical Society*, 507(1), 1216–1228. doi: 10.1093/mnras/stab2218
 860 Yao, Z., Bonfond, B., Clark, G., Grodent, D., Dunn, W., Vogt, M., ... Bolton, S.
 861 (2020). Reconnection- and Dipolarization-Driven Auroral Dawn Storms and Injections. *Journal of Geophysical Research: Space Physics*, 125(8). doi:
 862 10.1029/2019JA027663
 863 Yao, Z., Dunn, W., Woodfield, E., Clark, G., Mauk, B., Ebert, R., ... Bolton, S.
 864 (2021). Revealing the source of jupiter's x-ray auroral flares. *Science Advances*, 7(28), eabf0851. Retrieved from <https://www.science.org/doi/abs/10.1126/sciadv.abf0851> doi: 10.1126/sciadv.abf0851
 865 Yoshioka, K., Murakami, G., Yamazaki, A., Tsuchiya, F., Kagitani, M., Sakanoi,
 866 T., ... Yoshikawa, I. (2013). The extreme ultraviolet spectroscope for planetary science, EXCEED. *Planetary and Space Science*, 85, 250–260. doi:
 867 10.1016/j.pss.2013.06.021
 868
 869
 870
 871
 872
 873
 874
 875
 876
 877
 878
 879
 880

Figure 1.

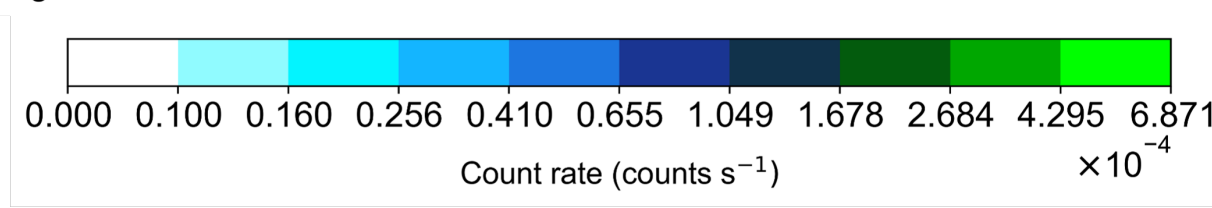
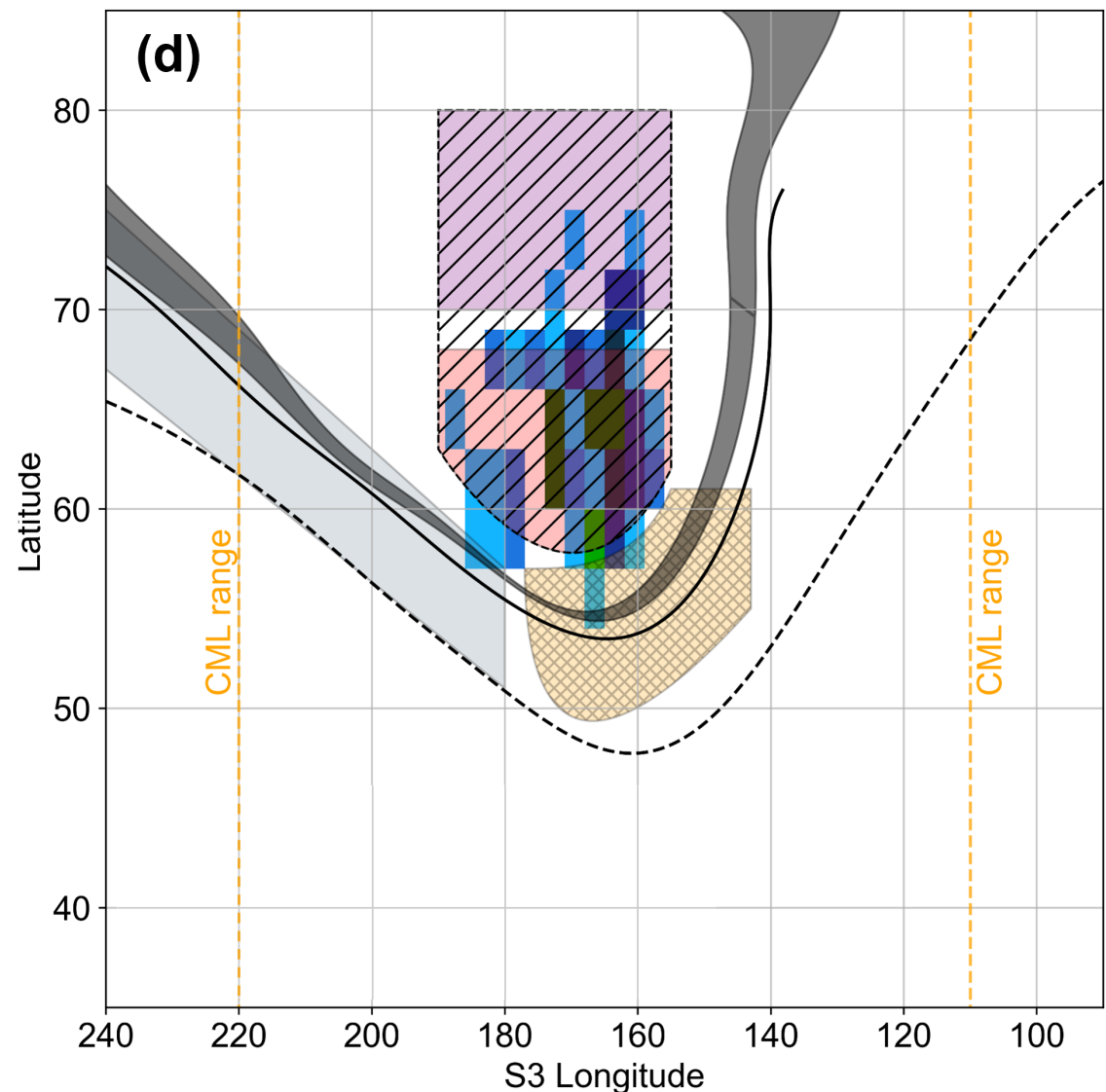
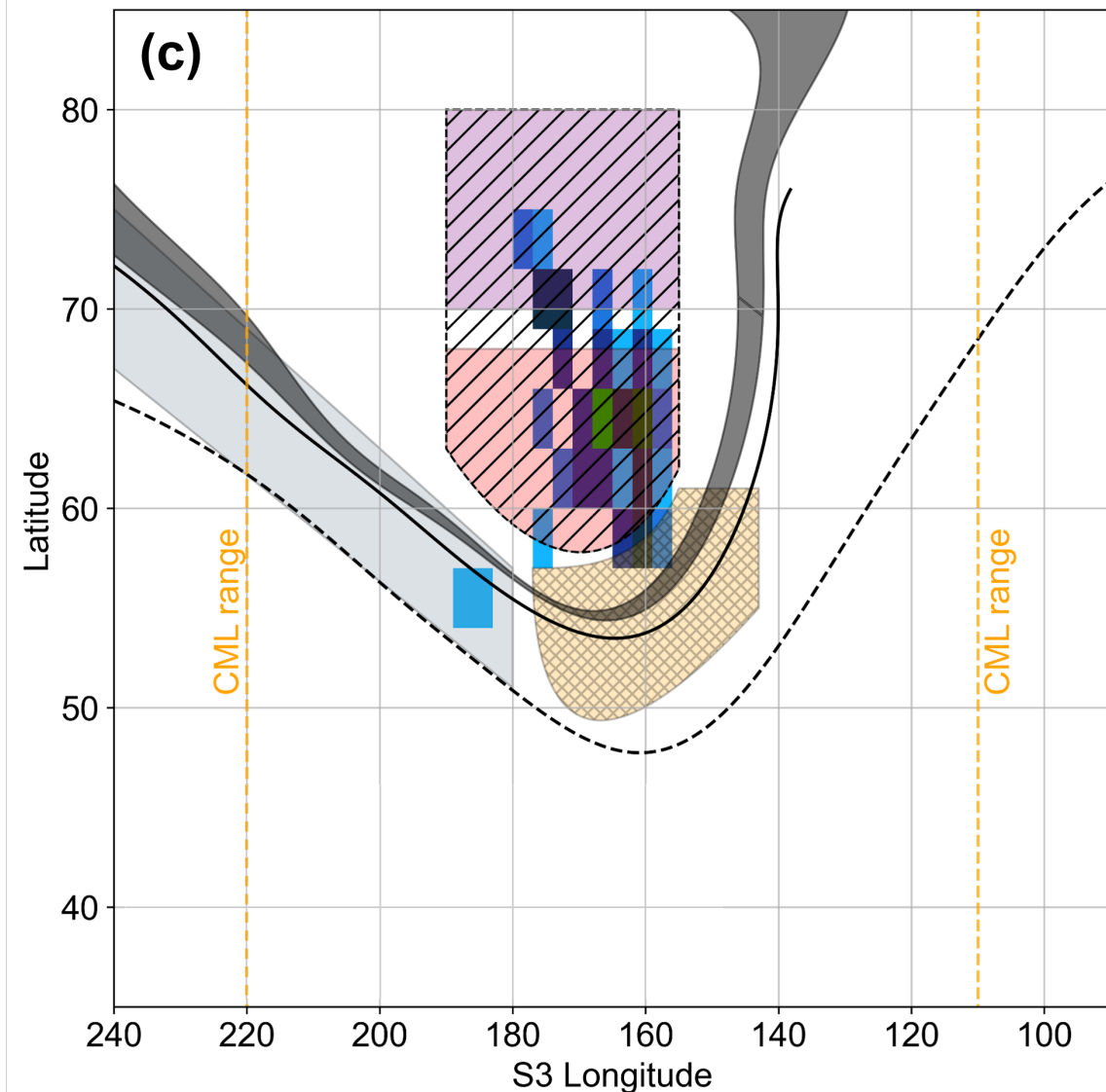
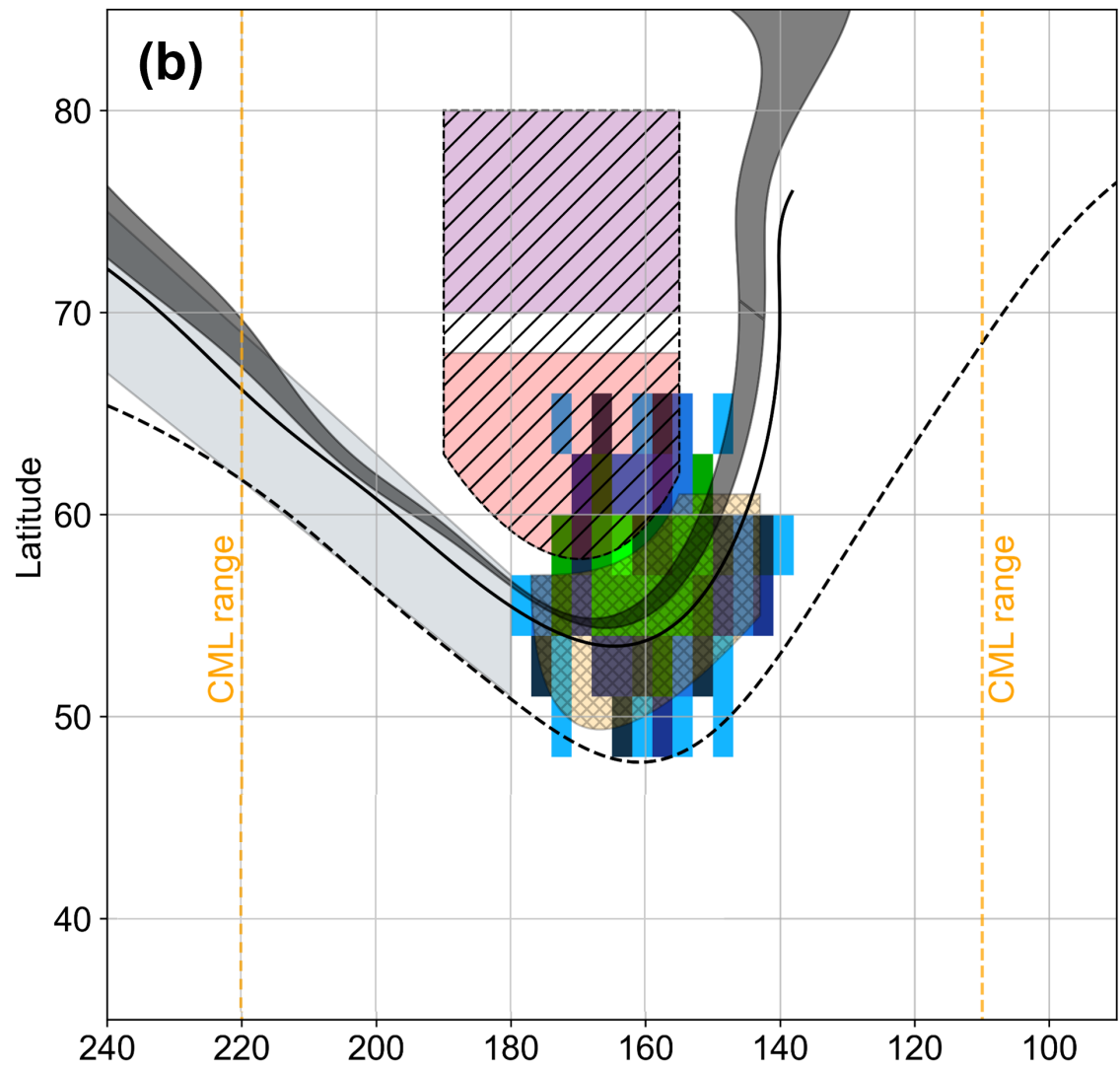
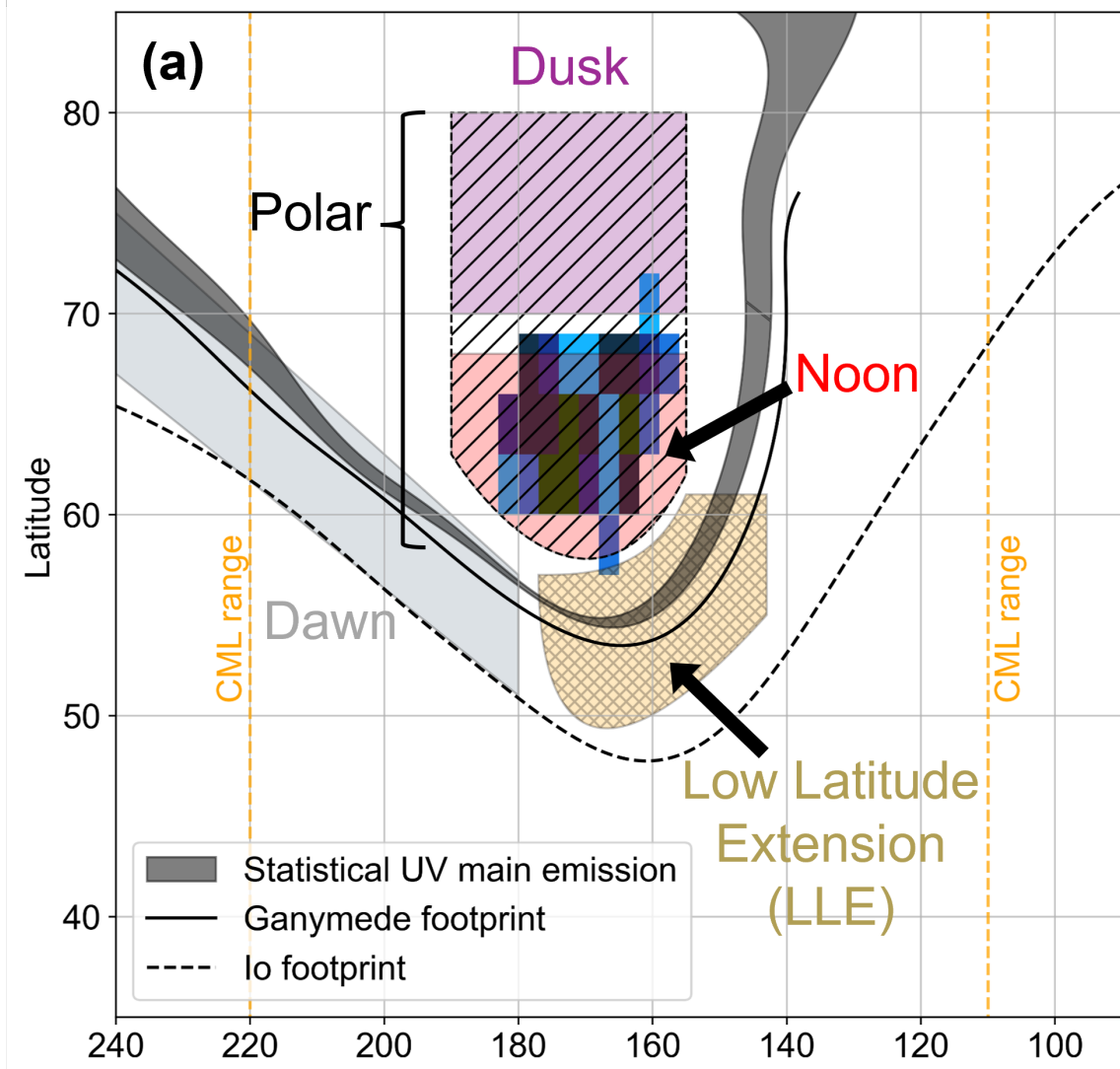


Figure 2.

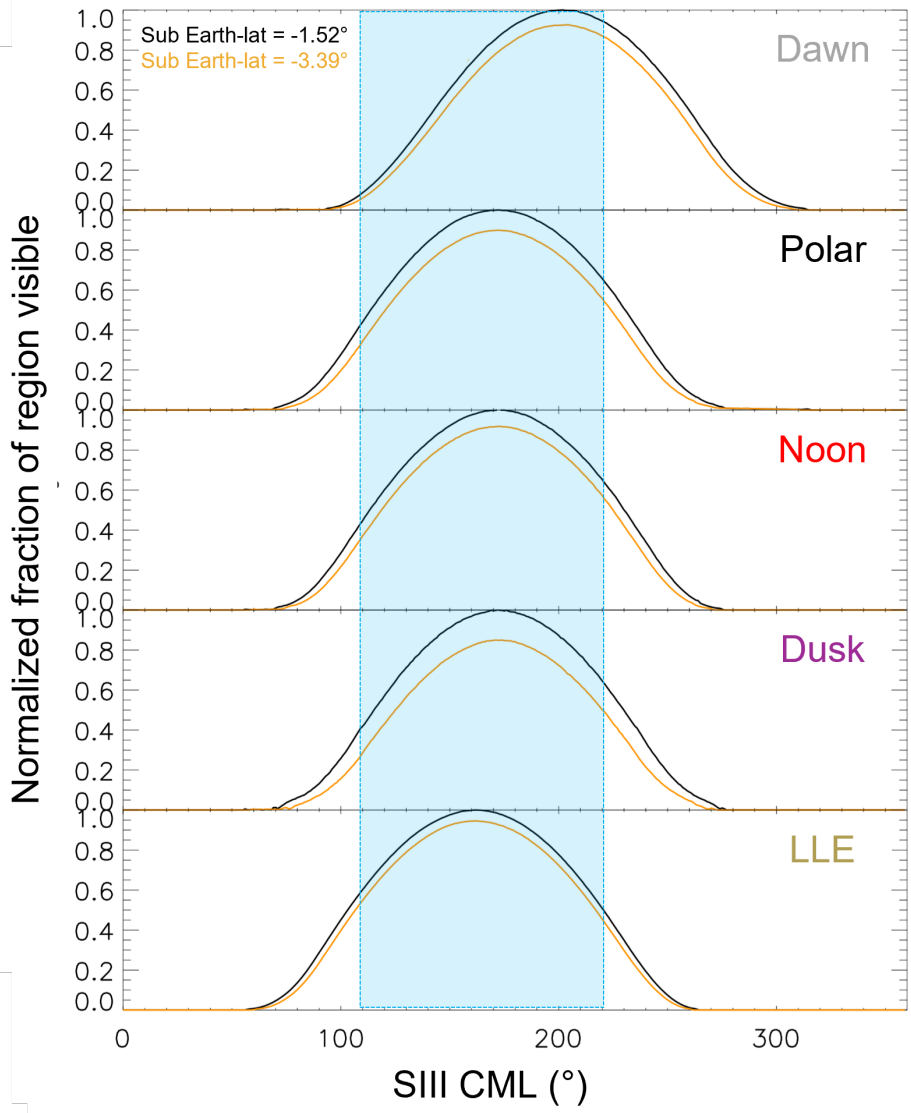


Figure 3.

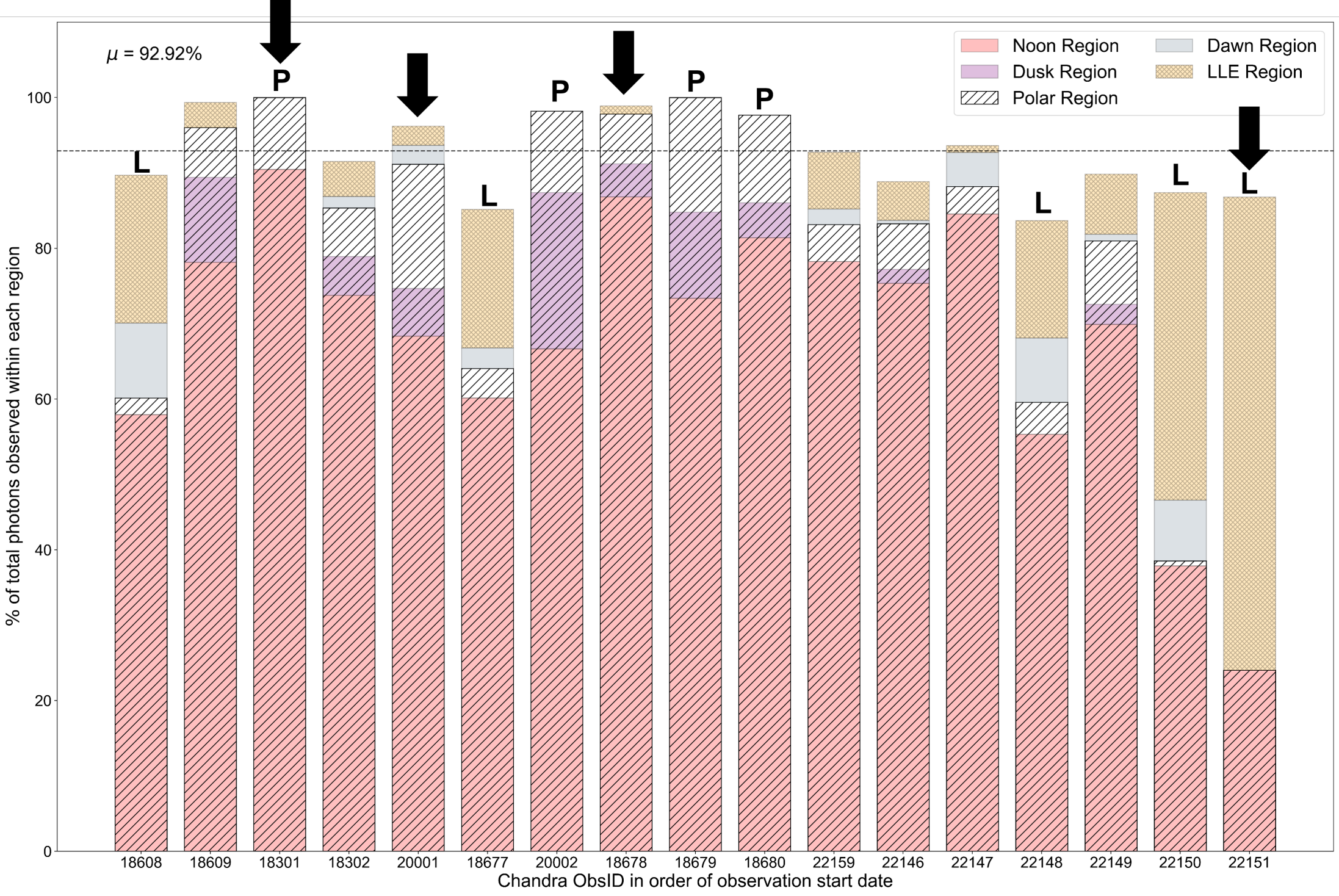
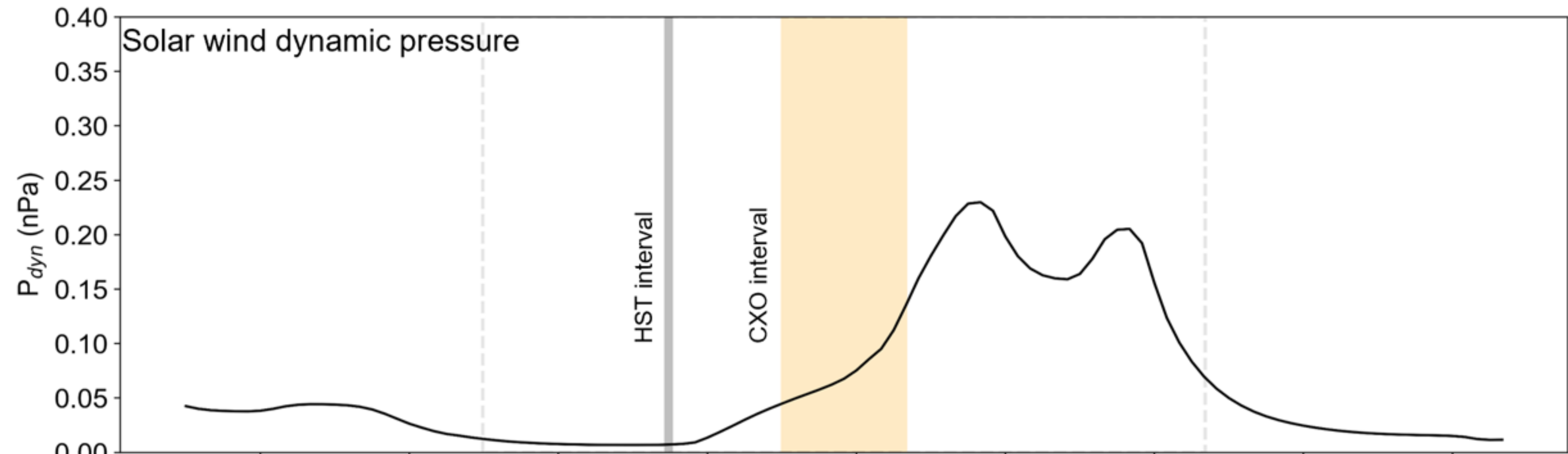


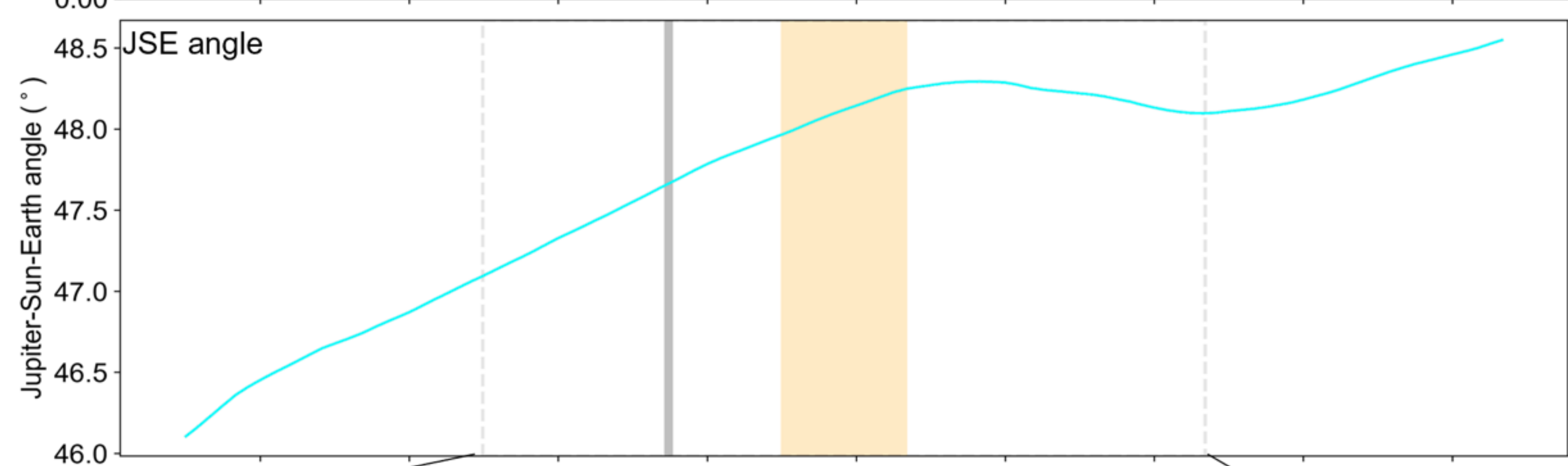
Figure 4.

(a)

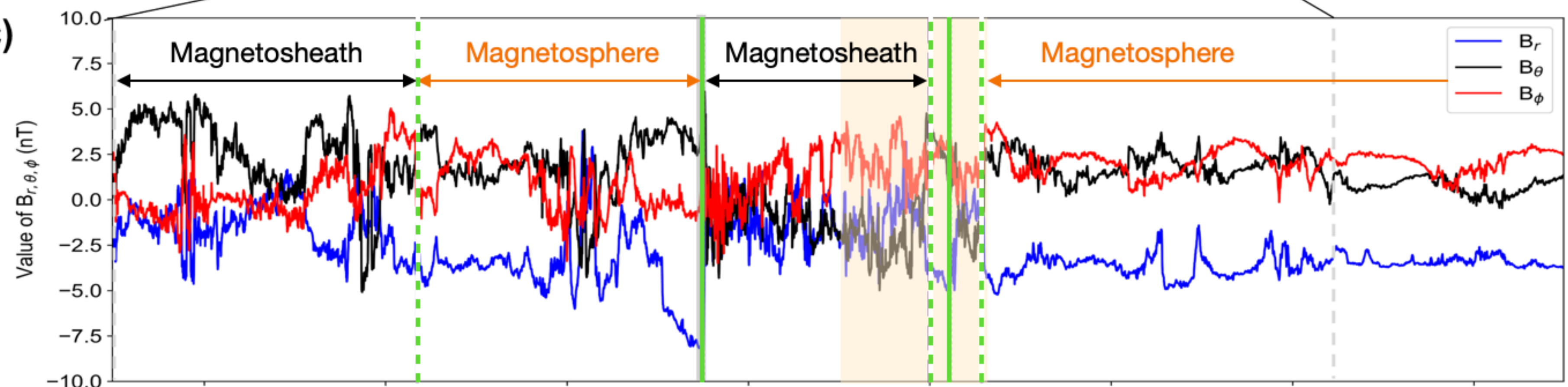
- G18 prediction
 - This study



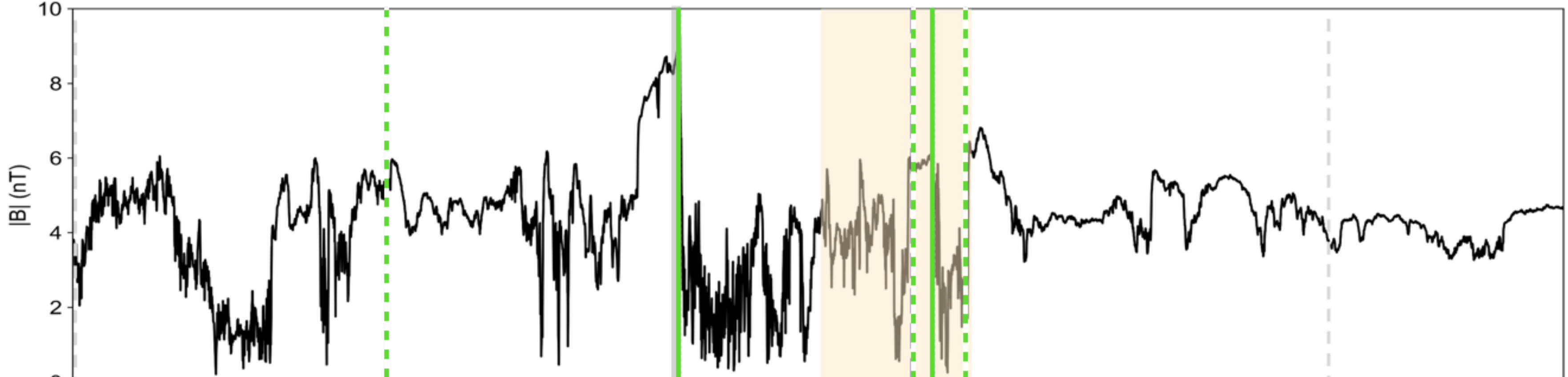
(b)



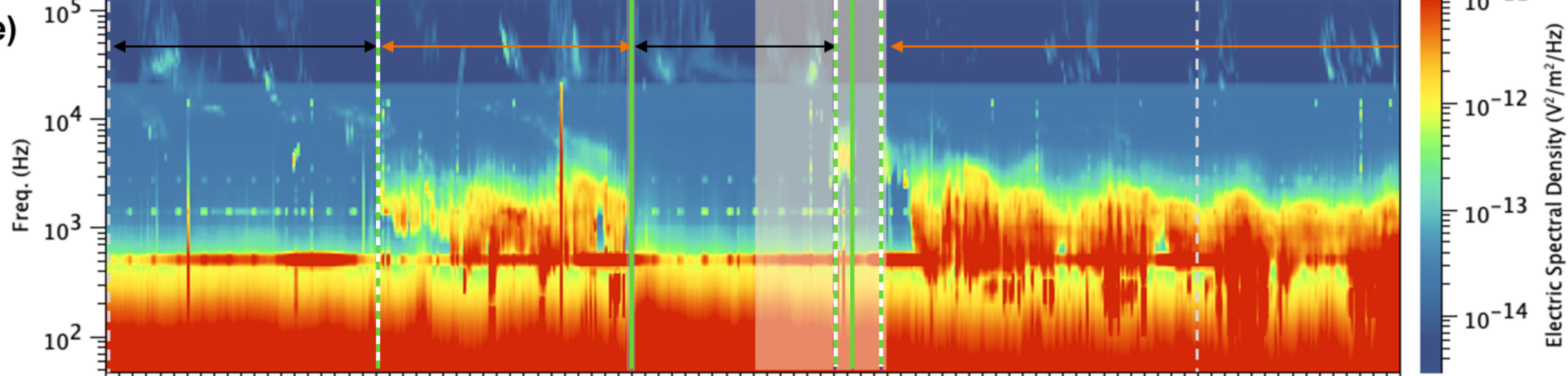
(c)



(d)



(e)



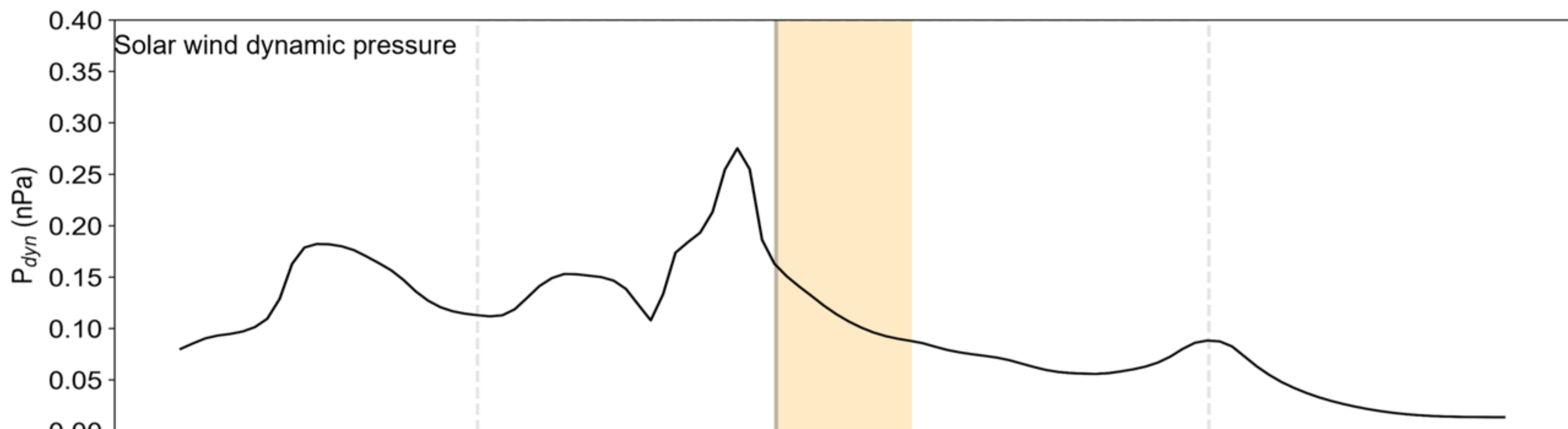
	00:00	12:00	00:00	12:00	00:00	12:00	00:00	12:00
Distance (R_J)	111.97	111.71	111.40	111.04	110.62	110.16	109.64	109.07
Lon (°)	147.30	222.60	297.80	13.12	88.40	163.70	238.90	314.20
Lat (°)	-8.02	-7.85	-7.68	-7.51	-7.34	-7.17	-7.00	-6.82
MLat _{JRM09} (°)	-1.24	1.44	-9.56	-17.80	-10.44	1.50	0.66	-11.49
MLT (hours)	4.39	4.46	4.50	4.41	4.24	4.42	4.43	4.49

2017-06-16 (167) 17:55 to 2017-06-20 (171) 17:56

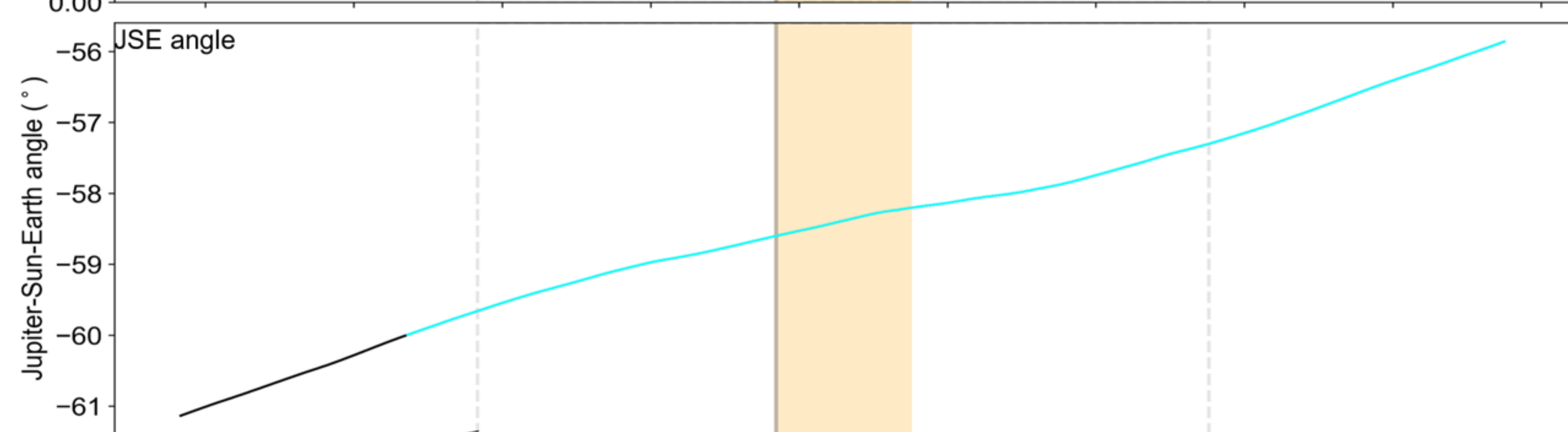
Figure 5.

(a)

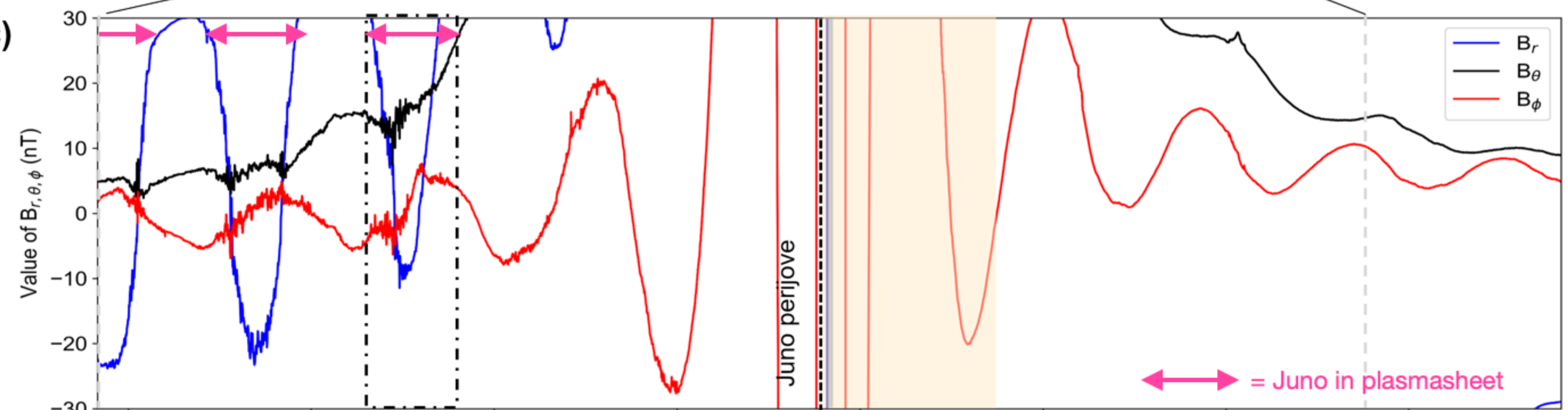
+ - This study



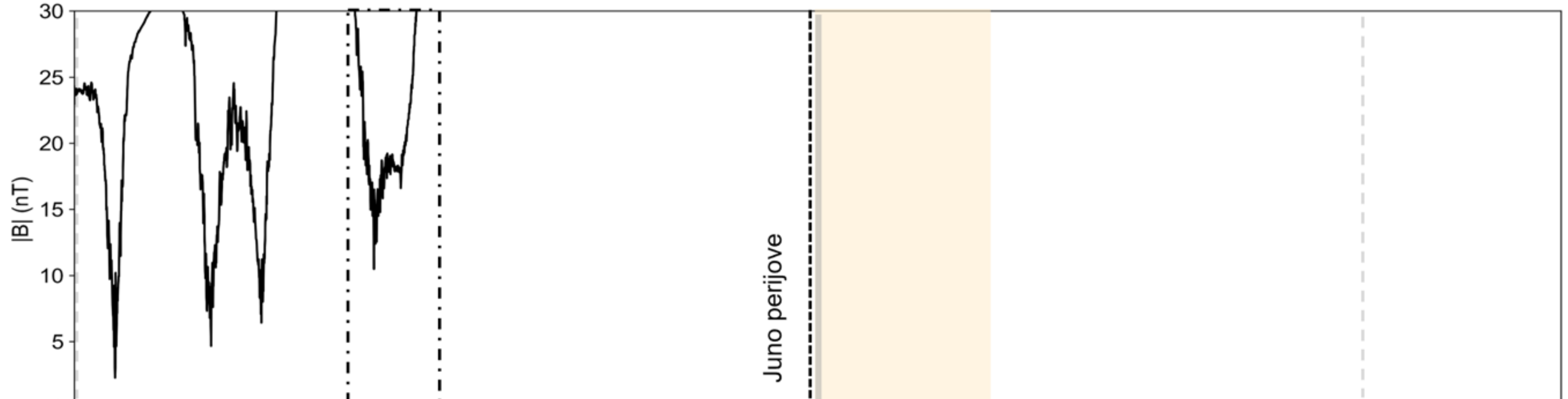
(b)



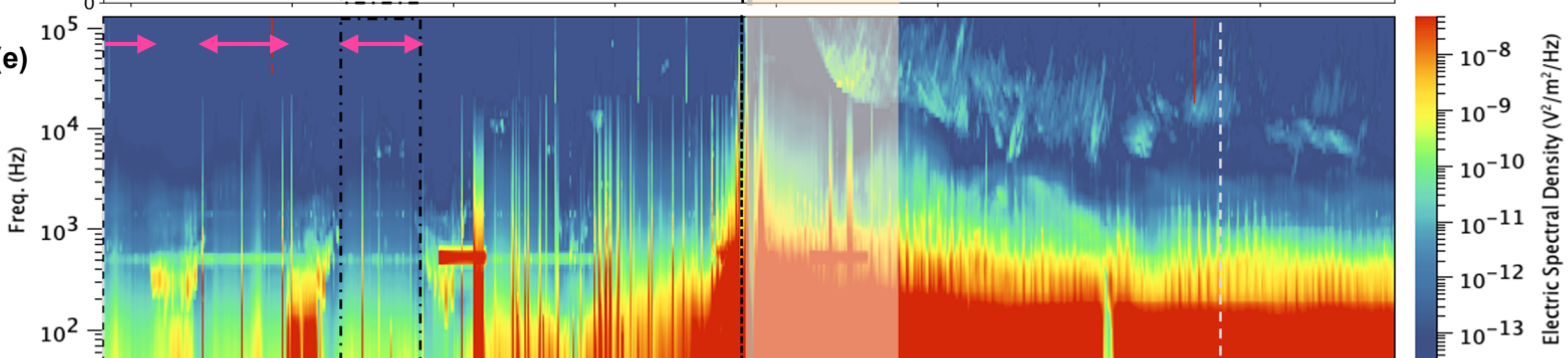
(c)



(d)



(e)



	12:00	00:00	12:00	00:00	12:00	00:00	12:00	00:00
Distance (R_J)	31.64	26.00	19.44	11.22	3.84	14.57	22.02	28.19
Lon _{III} (°)	76.85	152.40	228.10	304.50	354.00	86.77	163.20	239.00
Lat (°)	4.39	6.90	10.98	20.26	-74.71	-42.88	-36.53	-33.21
MLat _{JRM09} (°)	-0.76	14.22	19.71	16.81	-83.03	-45.56	-27.75	-25.36
MLT (hours)	2.86	2.96	2.79	2.54	6.75	2.60	3.02	3.48

2018-03-30 (089) 09:59 to 2018-04-03 (093) 09:59

Electric Spectral Density ($V^2/m^2/Hz$)